Chem Soc Rev

TUTORIAL REVIEW

View Article Online
View Journal | View Issue

Cite this: *Chem. Soc. Rev.*, 2022, **51**, 7732

Biodistribution, degradability and clearance of 2D materials for their biomedical applications

Taojian Fan, †[ab] Li Yan,†[a] Shiliang He,†[a] Qiancun Hong,[a] Fujin Ai,[a] Shuqing He,[a] Tao Ji,[a] Xin Hu,[a] Enna Ha,[a] Bin Zhang,[b] Zigang Li,[cd] Han Zhang, *[b] Xianfeng Chen *[e] and Junqing Hu *[ac]

Two-dimensional (2D) materials have evolved to be a class of rapidly advancing chemical entities in the biomedical field. Nevertheless, potential side effects and safety concerns severely limit their clinical translation. After administration, 2D materials cross multiple biological barriers and are distributed throughout the body. Only the portion that accumulates at the diseased sites exerts a therapeutic effect, whereas those distributed elsewhere may cause damage to healthy tissues and interference to normal physiological function of various organs. To achieve maximum therapeutic efficacy and minimum adverse effects simultaneously, the delivery of 2D materials must be targeted at diseased sites to reach therapeutic concentrations, and the materials must possess sufficient degradation and clearance rates to avoid long-term toxicity. Therefore, it is essential to understand the biodistribution and destiny of 2D materials *in vivo*. In this review, first, we provide a comprehensive picture of the strategies that are currently adopted for regulating the *in vivo* fate of 2D materials, including modulations of their size, surface properties, composition, and external stimuli. Second, we systematically review the biodistribution, degradation, and metabolism of several newly emerged 2D materials. Finally, we also discuss the development opportunities of 2D materials in the biomedical field and the challenges to be addressed.

Received 10th May 2022

DOI: 10.1039/d1cs01070k

rsc.li/chem-soc-rev

Key learning points

(1) Unique properties and applications of 2D materials in the biomedicine field.
(2) Biological barriers that 2D materials face *in vivo*.
(3) Tracking methods for the biodistribution of 2D materials *in vivo*.
(4) Degradation, metabolism and regulation strategies of 2D materials *in vivo*.
(5) Challenges and prospects of the clinical transformation of 2D materials.
This review focuses on recent advances in the biodistribution, biodegradation, and metabolic studies of 2D materials for their biomedical applications.

1. Introduction

With the rapid development of nanotechnology, increasing numbers of nanomaterials have shown unique advantages in the field of biomedicine and disease therapy. Among these candidate materials, 2D materials are attracting increasing attention as effective therapeutic and diagnostic agents, owing to their advanced properties and ultra-thin planar structure.[1] For example, 2D materials exhibit a large specific surface area and chemical active sites, which are highly beneficial for both drug loading and surface modification. Compared to traditional materials, some 2D materials exhibit ultra-sensitive responses to external stimuli, including lasers, X-rays, magnetic fields, and ultrasound.[2] 2D materials possess numerous excellent properties,

[a] College of Health Science and Environmental Engineering, Shenzhen Technology University, 518118, Shenzhen, China. E-mail: hujunqing@sztu.edu.cn
[b] Institute of Microscale Optoelectronics, and Otolaryngology Department of the First Affiliated Hospital, Shenzhen Second People's Hospital, Health Science Center, Shenzhen University, Shenzhen 518060, China. E-mail: hzhang@szu.edu.cn
[c] Pingshan Translational Medicine Center, Shenzhen Bay Laboratory, Shenzhen 518132, China
[d] Laboratory of Chemical Oncogenomics, School of Chemical Biology and Biotechnology, Peking University Shenzhen Graduate School, Shenzhen, 518055, China
[e] School of Engineering, Institute for Bioengineering, The University of Edinburgh, King's Buildings, Mayfield Road, Edinburgh EH9 3JL, UK. E-mail: michael.chen@ed.ac.uk
† These authors contributed equally to this work.

such as strong optical absorption, ultra-high photothermal conversion efficiency, and excellent quantum yield of active oxygen.[3] Owing to all of these advantages, they are widely used in numerous fields, such as photothermal therapy (PTT), photodynamic therapy (PDT), multimodal imaging, radiotherapy sensitization, drug delivery, cancer immunotherapy, and wound healing.[4]

Although significant advances have been made, the biological safety of 2D materials remains a crucial concern to be addressed before their clinical application. To avoid potential long-term toxicity, an ideal 2D material must be completely metabolized and excreted after treatment. Compared to organic materials, most inorganic materials face disadvantages in terms of biodegradation and metabolism.[5] Numerous researchers conducted in-depth studies on the degradation and metabolism of 2D materials. Newman *et al.* tracked the degradation process of graphene oxide (GO) *in vivo* for 270 days,[6] and observed that the Raman signal of GO in the spleen caused the largest loss within 1 month and became completely undetectable after 9 months. Jasim *et al.* performed a bladder puncture to obtain the most accurate and timely metabolic data,[7] showing that approximately 50–60% GO was found in urine within 2 h post-injection (PI). Besides metabolism, the biodistribution of 2D materials is another essential factor to consider, as the distribution across different organs reflects the metabolic approach of 2D materials. The blood circulation time is related to metabolism. In the design of the diagnosis and treatment platform based on 2D materials, it is crucial to maximize delivery to the diseased areas. A good targeting of the materials not only reduces the side effects induced by off-targeting but also significantly improves the therapeutic effect and reduces the cost. Owing to the flexible plane structure, 2D materials may undergo morphological reconfiguration when trespassing some barrier components.[7] Consequently, the biodistribution and metabolism of 2D materials differ from those of other biomaterials and can be rather complex.

This review focuses on recent advances in the biodistribution, biodegradation, and metabolic studies of 2D materials for their biomedical applications. First, the main regulation strategies of the *in vivo* fate of 2D materials are introduced. Second, the progress of understanding the *in vivo* behavior of a range of 2D materials is systematically summarized. Finally, the progress, challenges, and future prospects of this field are discussed.

2. The regulation strategies of *in vivo* 2D materials

The ultimate goal of drug delivery systems is to employ vectors to facilitate the accumulation of therapeutic agents at disease sites, with rapid degradation and metabolization of the vectors without side-effects. However, due to many barriers, most vector materials used in drug delivery systems accumulate in off-target tissues and organs.[8] For example, the first barrier is the protein corona, which is formed by proteins in bodily fluids that adsorb to the surface of the vector materials. Previous studies revealed that protein corona might reduce the blood circulation time of nanomaterials, resulting in poor biodistribution and masking of targeting ligands.[5] The properties of protein corona depend on the properties of 2D materials themselves and the body fluid environment at first contact. Therefore, tuning the size, shape, surface charge, and administration of 2D materials affects the protein corona. The second barrier that 2D materials must cross is the mononuclear phagocytic system (MPS), which includes monocytes in the blood and macrophages residing in tissues and sequesters most of the administered nanomaterials. For example, Kupffer cells line up inside the liver sinusoids to capture the passing nanoparticles. Consequently, the liver was found to be the main organ accumulating 2D materials.[9] In addition to biodistribution, the clearance of 2D materials is another issue that must be considered, as excretion of 2D materials after treatment can reduce potential long-term toxicity.

Taojian Fan was born in Hubei, China, in 1995, and is pursuing his Ph D degree under the guidance of Prof. Junqing Hu in the College of Health Science and Environmental Engineering, Shenzhen Technology University. His current research interests focus on two-dimensional material based theranostic nanoplatforms for biomedical applications.

Han Zhang received his PhD from the Nanyang Technological University in 2010. Currently, he is a full professor at the College of Optoelectronic Engineering at Shenzhen University in China. His main research interests are the application of two-dimensional nanomaterials in phototherapy and drug delivery. His publications have received >57 000 citations, with an H-index of 133 (according to Google scholar). He has been awarded as Highly Cited Researcher by Clarivate Analytics from 2018 to 2021.

Xianfeng Chen received his PhD from the University of Oxford. He is currently working in the Institute for Bioengineering in the School of Engineering at The University of Edinburgh as a Senior Lecturer (Associate Professor). Dr Chen's research is focused on biomaterials, biomedical engineering, and the application of nanomaterials in biology and medicine.

Junqing Hu received his PhD from University of Science & Technology of China (2000). He is a Full Professor at the College of Health Science and Environmental Engineering, Shenzhen Technology University. He has authored and co-authored more than 300 refereed journal publications and held over 60 patents. His current research interests focus on: (1) the design and functionalization of the NIR-responsive photothermal/photodynamic nanomaterials for biomedical applications and (2) the manipulation and measurements of individual nanostructures inside a TEM.

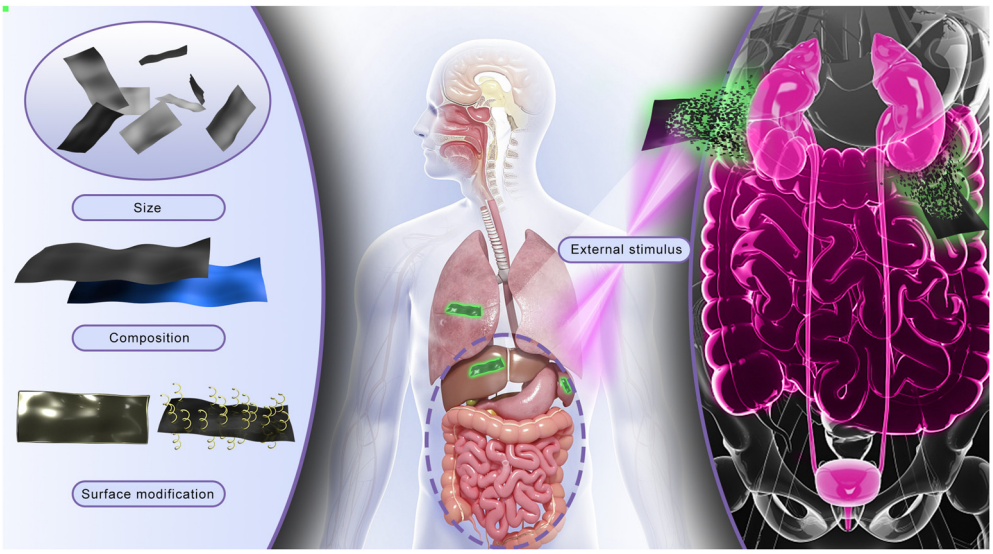

Fig. 1 Schematic diagram of the *in vivo* fate of 2D materials. 2D materials of suitable size, composition, and surface modification are fabricated for biomedical applications. After administration, 2D materials are distributed throughout the body, especially in the MPS-enriched organs. At this stage, external stimuli are applied to modulate the *in vivo* behavior of 2D materials. Eventually, 2D materials are degraded and excreted with feces and urine.

However, only nanomaterials smaller than 6 nm are effectively metabolized by the kidneys,[10] which is the most common metabolic pathway. To balance the therapeutic effect and metabolism of 2D materials, researchers have designed various

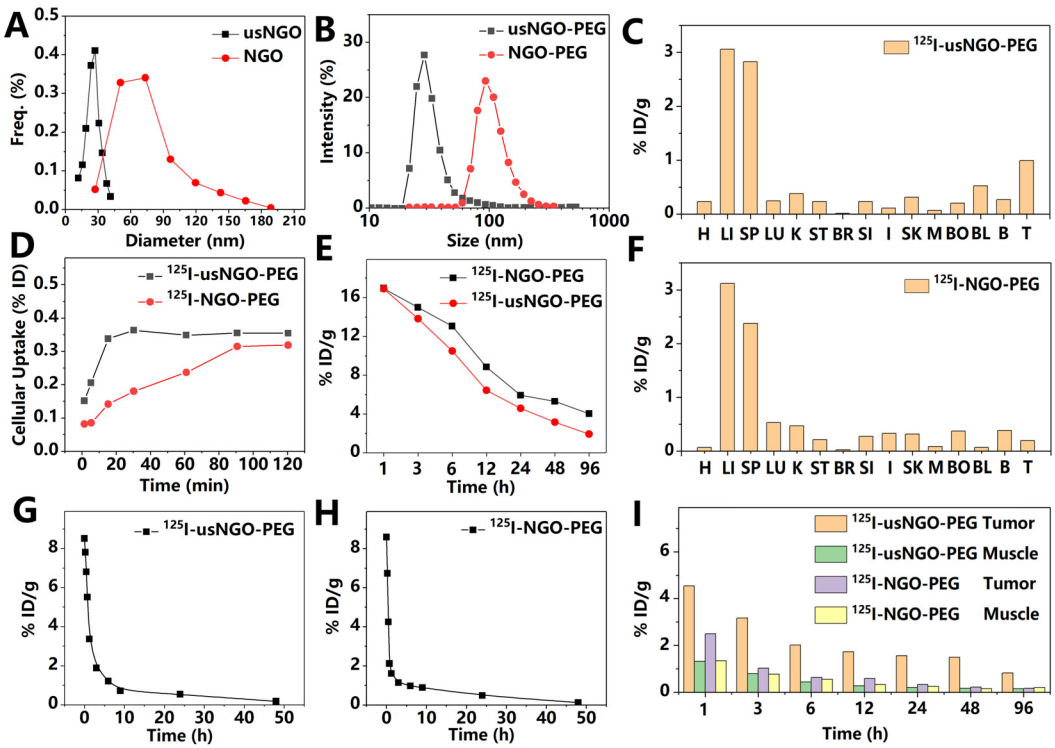

Fig. 2 (A) Size distribution of nano GO with normal (NGO) or ultra-small size (usNGO), based on atomic force microscopy results. (B) Hydrodynamic diameters of NGO and usNGO, measured by dynamic light scattering. (C and F) Biodistribution of usNGO (C) and NGO (F) 48 h PI. H: heart; LI: liver; SP: spleen; LU: lungs; K: kidneys; ST: stomach; BR: brain; SI: small intestine; I: large intestine; SK: skin; M: muscle; BO: bone; BL: blood; BLA: bladder; and T: thyroid. (D) Cellular uptake of NGO and usNGO. (E) Whole-body time-activity curves of NGO and usNGO after intravenous (i.v.) injection. (G and H) The blood circulation curve of usNGO (G) and NGO (H). (I) 4T1 tumor and muscle uptake for NGO and usNGO. Quantitative data in cells and *in vivo* mouse model were determined by the radioactive signal of ^{125}I-labeled materials. Adapted and modified with permission from ref. 11. Copyright (2016) Royal Society of Chemistry.

strategies to control the *in vivo* behavior of 2D materials, including the size, surface modification, element composition, and external stimulus, as shown in Fig. 1. In this section, the strategies of tuning the size, composition, surface modification, and external stimulus to regulate the *in vivo* fate of 2D materials are described in detail.

2.1 Size

The radial size of 2D materials significantly affects their interactions with the biological environment. As one of the most important properties, size dictates cellular uptake, biodistribution, circulation time, clearance routes, and blood–brain barrier (BBB) penetration of 2D materials. Generally, for the treatment and diagnosis of solid tumors, the most common size of 2D materials is <200 nm, which is beneficial to the passive targeting efficiency. Extensive research has been performed to determine the optimal delivery size of each type of 2D material. Cao *et al.*[11] compared the *in vivo* behavior of PEGylated GO nanosheets with sizes of 91 ± 34 nm and 28 ± 10 nm, as shown in Fig. 2. The *in vivo* data showed that small GO nanosheets led to 2–5 times higher accumulation at the tumor site than the large ones. The absorption of the small GO nanosheets in tumor and muscle tissues also showed better tumor specificity. Furthermore, the liver related-clearance of small GO nanosheets was significantly faster. Pharmacokinetic studies indicate that the blood circulation time of both small and large GO nanosheets was comparable (first phase half-lives: 0.8 ± 0.1 h for small GO nanosheets and 0.2 ± 0.1 h for large ones; second phase half-lives: 22.5 ± 4.9 h for small GO nanosheets and 26.7 ± 5.8 h for large ones).

Because size plays a key role in determining the absorption, uptake, and clearance of nanomaterials, the strategy of tunable size nanomaterial in the biological environment has been developed to enhance the therapeutic efficacy and safety profile. Accumulation at the target site and clearance after the treatment are two major factors that must be considered for highly efficient drug delivery. Unfortunately, these two aspects are sometimes contradictory. Because of excellent kidney metabolism, the residence time of ultra-small nanoparticles *in vivo* is too short for effective enrichment at the target site. One possible solution is to fabricate materials with a tunable size. Shao *et al.* exfoliated black phosphorus (BP) QDs with a size below 5 nm and modified it with PLGA.[12] PLGA nanospheres loaded with BPQDs showed a suitable size of about 102.8 ± 35.7 nm and significantly prolonged the blood circulation time compared to bare BPQDs. Gradually, the PLGA coating degrades *in vivo*, and ultra-small BPQDs are exposed and eliminated from the body. Similarly, BPQDs encapsulated by exosomes also exhibit enhanced passive tumor targeting due to their increased size.[13] Beyond natural biodegradation, nanomaterials can also be designed to respond to microenvironments in the human body, such that the size tunability is more flexible and rapid. To prolong retention in the tumor, Wang *et al.*[14] designed self-assembled BP nanosheets that activate in an acidic microenvironment. In their study, polyoxometalates modified BP nanosheets exhibited a small size ($\sim$205.4 nm) in the blood (pH = 7.4), while the size increased to 288 nm, which was triggered by an acidic microenvironment (pH $\approx$ 6.5) at the tumor site. After being endocytosed by tumor cells, the modified BP nanosheets self-assembled into micron-scale aggregates (835.3 nm) under the influence of the sharply decreased pH (pH = 5.5–3.0) of the intracellular compartment. The cellular uptake experiments confirmed that the modified BP nanosheets exhibit strong aggregation in cancer cells. The *in vivo* experiments demonstrated that the modification of polyoxometalate was helpful for the retention of BP nanosheets at tumor sites, indicating the great potential of microenvironment-activated self-assembly in tumor treatment.

2.2 Surface modification

Due to the large surface area of 2D materials, ions and proteins in the physiological environment are easily adsorbed on the material surface, causing agglomeration and coverage of the conjugated targeting ligands, which are designed to specifically target diseased areas.[15] In most research, surface modification is necessary to alleviate this problem. After modification, 2D materials exhibited extended blood circulation time, enhanced macrophage escape, improved targeting ability, and controllable stability.[16] Most modifications enhanced the biocompatibility and dispersibility of 2D materials under physiological conditions. PEG, polydopamine, cell membrane, and peptides are the most commonly used modification strategies for 2D materials. For example, after incubation in phosphate buffered saline (PBS), serum, or cell culture medium for 24 h, bare Sb nanosheets completely precipitated, while PEG-coated Sb nanosheets remained stable.[17] For easily degradable 2D materials, modification can also help control the degradation rate. Zeng *et al.*[18] coated polydopamine on the surface of BP nanosheets to improve their stability by the polymerization effect of dopamine under weak alkaline conditions. After being stored in water for 3 days, the photothermal performance (the temperature increase induced by the photothermal effect of BP) of the modified BP and bare BP attenuated by 2.8 °C and 5.4 °C, respectively. The polydopamine coating reduced the contact of BP nanosheets with oxygen, thereby slowing down the degradation rate. In another study, Sun *et al.*[19] used the electrophilic titanium ligand (TiL_4) to deprive BP of its lone pair of electrons to reduce the reaction between BP and oxygen, as shown in Fig. 3A. This was demonstrated by measuring the UV-vis absorption of the materials. After exposure to air for 10 days, the absorption of pure BPQDs was dramatically reduced by 43%, while that of the TiL_4 modified BPQDs was only reduced by 10%. In addition, the modified BPQDs showed significantly improved dispersion in the cell culture medium. Furthermore, TiL_4 also changed the surface potential of BPQDs. The potentials of BPQDs before and after modification were -36.5 ± 1.1 and $+21.1 \pm 2.56$ mV, respectively. The positive potential of BPQDs may be beneficial to the cellular uptake of tumor cells due to the negative surface potential of cell membrane. The maximum photoacoustic (PA) signal in the tumor site was detected at 4 h after tail vein injection of TiL_4-coated BPQDs, and the PA signal returned to a low level at 48 h after the injection, indicating the rapid clearance.

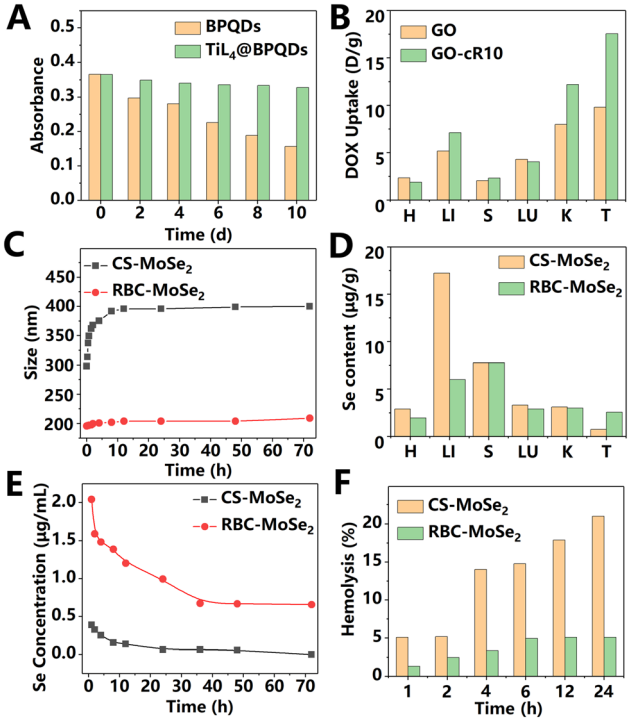

Fig. 3 (A) Change in the absorption intensity of BPQDs and TiL_4 @ BPQDs in water. Test wavelength is 450 nm. Adapted and modified with permission from ref. 19. Copyright (2017) Wiley-VCH Verlag GmbH & Co. KGaA, Weinheim. (B) Quantitative biodistribution of DOX in mice at 24 h post i.v. administration of GO or Cyclic R10 Peptide-modified GO (GO-cR10). Due to the nuclear targeting of Cyclic R10 Peptide, GO could release drugs in the nucleus under irradiation and avoid the "efflux pump" on the plasma membrane. H: heart; LI: liver; S: spleen; LU: lung; K: kidneys; and T: tumor. Adapted and modified with permission from ref.22 Copyright (2020) Wiley-VCH Verlag GmbH & Co. KGaA, Weinheim. (C) Time-dependent size of CS-$MoSe_2$ or RBC-$MoSe_2$ nanosheets (20 μg mL^{-1}) dispersed in serum. (D) Biodistribution of $MoSe_2$ modified with red blood cell (RBC) membrane or chitosan (CS). (E): Time-dependent selenium content in mouse plasma after i.v. injection of CS-$MoSe_2$ or RBC-$MoSe_2$. (F) Hemolysis caused by CS-$MoSe_2$ or RBC-$MoSe_2$ at a concentration of 20 μg mL^{-1}. Adapted and modified with permission from ref. 20 Copyright (2019) Wiley-VCH Verlag GmbH & Co. KGaA, Weinheim.

Phagocytes may trap nanosheets and cause negative effects, such as decreased therapeutic efficiency and inflammation. In recent years, researchers found that cell membrane coating can effectively protect nanomaterials from being cleared by phagocytes. A variety of biofilms have been used to coat nanosheets and significantly improve the blood circulation time of materials. In 2019, He *et al.*[20] designed $MoSe_2$ nanosheets encapsulated with red blood cell membranes for photothermal-triggered cancer immunotherapy, as shown in Fig. 3C–F. After modification, the uptake of $MoSe_2$ nanosheets by macrophages was significantly reduced, which was related to the interaction between the self-marker and protein-alpha receptor on the surface of the red blood cell membrane. Compared with the control group, modified $MoSe_2$ nanosheets showed a very low hemolysis rate (less than 5%) and negligible protein corona, indicating a significantly improved blood compatibility. According to the results of biodistribution analysis, membrane modification helped nanosheets to escape the capture of macrophages in the liver and therefore improved accumulation of the $MoSe_2$ nanosheets at the tumor site. Due to the presence of red blood cell membranes, $MoSe_2$ nanosheets exhibited a drastically reduced blood clearance rate (the modified group: 0.1 μg ((μg mL^{-1}) h)$^{-1}$ *vs.* the unmodified group: 3.1 μg ((μg mL^{-1}) h)$^{-1}$ and significantly improved blood circulation half-life period (the modified group: 7.2 h *vs.* the unmodified group: 2.4 h). In addition to red blood cells, exosomes can also effectively improve the blood circulation time and tumor enrichment efficiency of 2D materials. Liu *et al.*[13] prepared exosome-encapsulated BPQDs. The renal clearance rate of exosome-encapsulated BPQDs with a size of about 100 nm was significantly slower than that of bare BPQDs with a size of less than 5 nm. The fluorescence images at 24 and 48 h PI demonstrated that the biodistribution of the encapsulated BPQDs was similar to that of pure exosomes. After 48 h of administration, the strongest fluorescence signal intensity of encapsulated BPQDs was observed in the spleen. The lungs, liver, and tumor sites also showed evident signals of BPQDs, while the signal in the heart and kidneys was very weak. In the fluorescence image of frozen sections, the co-localization of exosomes and tumor cell nuclei demonstrated the effective penetration of exosome-encapsulated BPQDs in tumor tissues. Afterwards, the photothermal performance of this material was investigated on the first and seventh days PI. The temperature increase of bare BPQD treated group was similar to that of exosome-encapsulated BPQDs on the first day. However, on the seventh day, the encapsulated BPQDs could still exhibit effective photothermal effects at the tumor site; while the bare BPQD group showed significant photothermal degradation. This phenomenon indicates that exosomes could extend the accumulation life time of BPQDs at the tumor site.

Compared with normal tissues, the tumor microenvironment differs in numerous aspects, such as the pH value, glucose concentration, hydrogen peroxide (H_2O_2) content, and expression of glutathione. Therefore, modification strategies triggered by the tumor microenvironment have been proven to effectively regulate the *in vivo* behavior of 2D materials. Mei *et al.*[21] anchored glucose oxidase on MoS_2 nanosheets for glucose-based tumor catalytic therapy. The modification changed the surface potential of MoS_2 nanosheets from −35 to +36 mV, which was conducive to the combination of nanosheets and negatively charged plasma membranes. The high content of glucose at the tumor site was catalyzed by glucose oxidase to H_2O_2, which was further converted to $^{\bullet}OH$ by MoS_2 nanosheets. The $^{\bullet}OH$ could not only kill cancer cells but also accelerate the degradation of nanosheets. Hence, almost no Mo element was detected in the main organs of animals that received the intratumor injection, indicating the accelerated *in vivo* clearance of the modified MoS_2 nanosheets. Although multiple targeting strategies have been developed to enhance the drug delivery capabilities of 2D materials, the "efflux pump" on the plasma membrane of cancer cells protected them from drugs. To solve this problem, Tu *et al.*[22] modified the Cyclic R10 peptide on the surface of graphene and observed significantly enhanced cell internalization, as shown in Fig. 3B. Cyclic R10 peptide is a cell-penetrating peptide containing 10 arginine residues. Its cyclic

structure effectively improves nuclear targeting ability. After modification, the efficiency of graphene entering HeLa-R cells was increased 10-fold. The *in vivo* fluorescence data of the labeled material showed that the modification significantly enhanced the enrichment of graphene in tumors and organs, which may be related to enhanced cell internalization. In addition, the content of the modified graphene accumulated in the tumor site was significantly higher than that in other organs, such as the liver, kidneys, and lungs. Impressively, compared to pure drug, the graphene drug delivery platform showed negligible toxicity on important indicators, including weight loss and cardiotoxicity.

2.3 Composite materials

In vivo behavior of materials is related to the materials' elemental composition and density.[23] A heterojunction is one of the most common approaches to change the composition of materials. Heterojunction material can synergize the advantages of each component and avoid its own shortcomings to a certain extent. For example, carbon dot/WS_2 heterojunctions were reported to have significantly enhanced passive targeting efficiency, great photothermal performance in the second near-infrared region, and physiological stability compared to a single component.[24] At 24 h after the tail vein injection, the fluorescence signal intensity of the heterojunction material at the tumor site reached its maximum, which was significantly higher than that of normal organs. Using CT imaging, it was found that heterojunctions gathered at the tumor area, and the amount was significantly higher than pure WS_2.[25] This demonstrated that the heterojunction changed the biodistribution of materials. In addition, constructing heterojunctions is a common method to control the stability of 2D materials. Huang *et al.*[26] fabricated Bi_2O_3/BP heterojunctions by growing Bi_2O_3 nanoparticles *in situ* on the surface of BP nanosheets. After being placed in water for 8 days, the Bi_2O_3/BP heterojunction dispersion did not change significantly. As a comparison, most pure BP was degraded in water, indicating the significantly enhanced stability of the heterojunction, as shown in Fig. 4. The increased stability prolonged the residence time *in vivo*. At 28 days after injection, the Bi element could still be detected in the liver and spleen. The enhanced stability raises the risk of potential long-term toxicity, but facilitates long-lasting therapeutic effects of BP nanosheets. Therefore, the Bi_2O_3/BP heterojunction and pure BP nanosheets can meet the needs of different diseases.

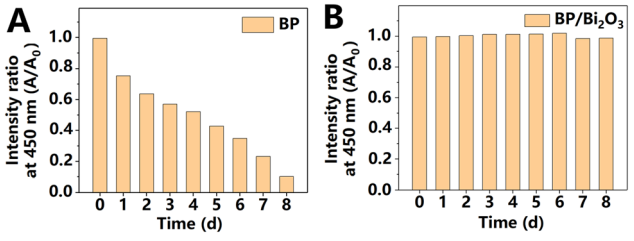

Fig. 4 Variations in the absorption intensity ratio at 450 nm of BP (A) and BP/Bi_2O_3 heterostructures (B) after standing in water for different durations of time. Adapted and modified with permission from ref. 26 Copyright (2018) Elsevier.

Another efficient approach to fabricate 2D composites is to design core–shell structures. For example, Tang *et al.*[27] developed a dense gold shell outside the Ti_3C_2 nanosheet core (Ti_3C_2@Au) by a seed growth method. In this work, SH-PEG was modified on the Au shell through gold–thiol bonds, which prevented the coordination of Ti_3C_2 nanosheets with the polymers in the physiological environment. As a result, this composite exhibited better dispersion in the physiological environment than bare Ti_3C_2. After i.v. injection, the core–shell Ti_3C_2–Au composite showed a long blood circulation time and significantly enhanced tumor enrichment compared to bare Ti_3C_2.

In addition to heterojunction and core–shell structures, other 2D composites also exhibit different degradation and *in vivo* behaviors from each component. Liang *et al.*[28] prepared rGO/BP hybrids, which possessed significantly enhanced stability in comparison with pure BP. The phosphorus–carbon covalent bond formed between rGO and BP pre-occupied the lone pair of electrons of BP and inhibited the oxidation of BP. The as-prepared hybrids were stable for over 30 days under ambient conditions. After encapsulation with PEG, the rGO/BP hybrids exhibited good dispersion in the physiological environment for four days without significant degradation and precipitation. Overall, these composite materials can not only improve the stability of easily degradable materials but also accelerate the biodegradation of stable materials. In another study, researchers designed composite materials based on the iron oxide nanoring and GO with a hydrodynamic size of ~166.6 nm.[29] Due to its attractive electrical and thermal conductivity, GO can improve the poor dielectric loss of magnetic particles and achieve enhanced magnetothermal performance. Furthermore, the significantly enhanced reactive oxygen species (ROS) production and immunological effects compared to those of pure iron oxide nanorings also indicate the advantages of this composite material in cancer magnetotherapy. Impressively, the analysis of the results of inductively coupled plasma mass spectrometry (ICP-MS) and magnetic resonance imaging (MRI) indicated that the material may degrade 48 h after i.v. injection. Elevated Fe content was found in the bile and urine of the treated mice, indicating that the degraded GO composite material is metabolized through the liver and kidneys. This result indicates that the construction of composites may improve the biodegradability of GO nanosheets, which is one of the main factors limiting the clinical application of GO. The MRI imaging data showed that the optimal time to apply a magnetic field was at 4 h after the administration, when the accumulation of the composite material at the tumor site reaches the maximum. By comparing the MRI signals of the liver, spleen, kidneys, gallbladder, and bladder of the mice treated with iron oxide nanoring and GO composite, researchers found that the liver and spleen accumulated GO composites the most. For the liver, spleen, and kidneys, the strongest material signal appeared at 8 h after administration. Compared with pure GO, the accumulation of the composite material in the heart and brain was significantly higher.[1] Therefore, the composite material may have more potential than pure GO for the treatment of heart and brain diseases.

In general, numerous studies proved that heterojunctions and composite materials exhibit significant differences from

the original components in terms of their biodistribution, degradation rates, and metabolic pathways *in vivo*. At present, in most designs of composite 2D materials, researchers are dedicated to improving the physical and chemical properties of materials, whereas the interaction between materials and organisms is often overlooked. To meet the clinical needs, more attention must be paid to the biological effects of materials.

2.4 External stimulus

2D materials show a sensitive response to external stimuli. Therefore, researchers can rationally control the fate of materials *in vivo* through multiple stimuli such as laser, ultrasound, and magnetism. For example, the local high temperature or the ROS induced by external stimuli can also significantly accelerate the degradation rates of some 2D materials, which has been applied on graphene oxide.[30] In a recent study, Lee *et al.*[30] designed a photo-switch strategy to generate oxidants, which induced the degradation and clearance of GO after treatment. In this system, the degradation of GO was accelerated by hypochlorous acid, which was catalyzed by the complex of specific single-stranded DNA (ssDNA) on the surface of GO with hemin. Before illumination, the ssDNA and its complementary strand formed a double-stranded DNA (dsDNA) without catalytic activity, which was corresponding to the OFF state. Under irradiation, the photothermal effect of GO melted the dsDNA into ssDNA, which then formed a complex with hemin with catalytic activity. Ultimately, the ssDNA-based complex produced hypochlorous acid and induced the degradation of the GO nanosheets. In this work, controllable biodegradation was achieved through the synergy of the photothermal effect of GO (key) and DNA double strands (lock). Meanwhile, physical stimulations can also enhance the permeability of blood vessels and increase the enrichment of materials in the lesion. As one example, upon exposure to the near-infrared region (NIR) light, 2D materials could significantly enhance the permeability of the BBB owing to the photothermal effect, which is of great significance in brain-related diseases. Xiong *et al.*[31] found that, under NIR irradiation, the BP nanosheets' penetration efficiency to an *in vitro* BBB model increased by a factor of two, as shown in Fig. 5A and B. Compared with the control group, the brains of mice that underwent the BP-based photothermal treatment showed significantly stronger blue staining in the Evans blue staining experiment, which proved that NIR light could evidently promote the brain delivery of the material. The fluorescence image showed that the nanosheets reached the brain 4 h after injection and achieved the peak at 6 h after injection. In addition, NIR irradiation also effectively prolonged the retention time of the material in the brain. Owing to the NIR-enhanced BBB penetration, 2D materials showed great application prospects in various brain diseases, including Parkinson's disease, Alzheimer's disease, and depression.[32–34] Moreover, NIR induced permeability enhancement is also useful in tumor therapy. Tao *et al.*[17] compared the penetration ability of DOX-loaded Sb nanosheets with and without irradiation. They found that light induced local heating of the cytomembrane increased membrane permeability and enhanced cell uptake of Sb nanosheets. Consequently, a strong DOX fluorescence signal

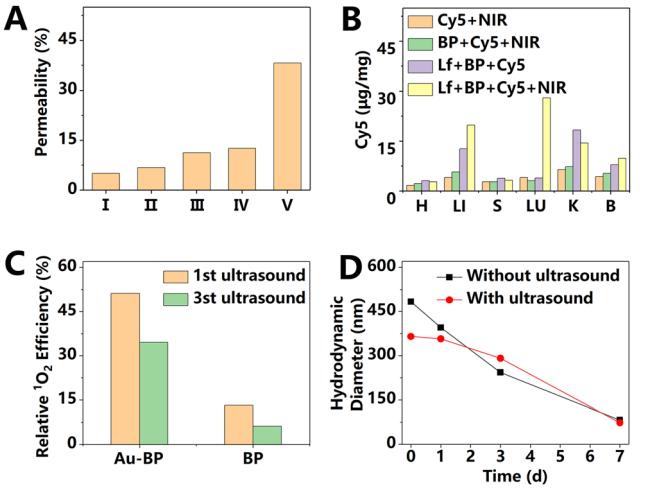

Fig. 5 (A) Permeability of *in vitro* BBB to BP. I: Cy5, the fluorescent label; II: BP + Cy5; III: BP + Cy5 + NIR; IV: Lf + BP + Cy5; and V: Lf + BP + Cy5 + NIR. Lf represents brain-targeting ligand lactoferrin. (B) Biodistribution of BP *in vivo* with or without irradiation on brain site. H: heart; LI: liver; S: spleen; LU: lungs; K: kidneys; and B: brain. Adapted and modified with permission from ref.31. Copyright (2020) Elsevier. (C) Relative $^1O_2$ efficiency of BP and Au–BP under first and third ultrasonic treatment (1 W cm^{-2}, 3 min). Concentration of BP is 1 μg mL^{-1}. (D) Hydrodynamic diameter of Au–BP with or without ultrasonic treatment (1 W cm^{-2}, 3 min) at different time points. Adapted and modified with permission from ref. 37 Copyright (2021) American Chemical Society.

was detected in the center of the tumor sphere treated with irradiation, while the DOX signal in the non-illuminated group was almost concentrated in the outer ring of the tumor sphere. Fu *et al.*[35] found that the degradation rate of MoS_2 was related to numerous factors, such as NIR irradiation, pH value, and H_2O_2 concentration. The MoS_2 dispersions changed from grayish black to colorless after 10 days of NIR irradiation (5 min of irradiation every 2 days, 1.0 W cm^{-2}), indicating the accelerated degradation rate. The researchers also compared the degradation of MoS_2 in the simulated body fluid (pH = 7.4), tumor microenvironment (pH = 6.0), and lysosomal fluid conditions (pH = 4.5). Under the condition of pH = 4.5, MoS_2 showed the fastest degradation. The presence of H_2O_2 could further shorten the time required for MoS_2 degradation. In the group with the fastest degradation rate (H_2O_2 + NIR, pH = 4.5), the size of MoS_2 decreased from 100–200 nm to 20–60 nm within 5 days, and it completely disintegrated into 5 nm particles within 10 days. This study thus shows that by regulating irradiation, 2D materials can be rapidly biodegraded under lysosomal fluid conditions.

Although the 2D materials triggered by NIR light exhibited numerous unique advantages, their penetration depth limits clinical application. To solve this problem, researchers made use of ultrasound as an external stimulus, as it reaches deep tissues. Dai *et al.*[36] loaded TiO_2 on the surface of reduced graphene oxide (rGO) nanosheets for enhanced sonodynamic therapy. Owing to the great electrical conductivity and 2D planar π-conjugated structure of rGO, the excited electrons of TiO_2 can be transferred from the conduction band to rGO through a percolation mechanism. As a result, charge recombination was

inhibited, enhancing generation of ultrasound-induced ROS. The biodistribution studies indicated that nearly 10% of the material accumulated at the tumor site. The blood circulation half-life of this GO composite was measured to be 0.8 h, and the elimination rate constant at 2 h after injection was -0.014 μg mL^{-1} h^{-1}. After treatment, the tumor inhibition rate of the experimental group reached nearly 78%, indicating the excellent anti-cancer effect of sonodynamic therapy based on 2D materials. In another study,[37] Chen *et al.* used Au-modified BP nanosheets as sonodynamic agents for breast cancer therapy. They found that the sonodynamic performance of BP was significantly decreased after three sonications, indicating ultrasound-induced degradation of BP, as shown in Fig. 5C. Although the Au-modified BP showed improved stability, its diameter decreased within 3 days under sonication treatment compared with the control group, as shown in Fig. 5D. During this process, the rapid degradation of BP may be attributed to the defects on the surface oxidized by the sonication-induced ROS. This ultrasound-controlled biodegradation effectively avoids the potential toxicity caused by the long-term retention of 2D materials *in vivo*, while ensuring the therapeutic effect.

In summary, various strategies have been used to control the fate of 2D materials *in vivo*, and several developments have been made. Notably, the optimal design differs for different 2D materials. Therefore, to achieve efficient and safe drug delivery, the *in vivo* behavior of each specific 2D material must be carefully studied, which we review in Section 3.

3. The *in vivo* fate of various 2D materials

In the past 10 years, 2D materials have expanded past graphene to form a large family. Owing to their planar structures, 2D materials exhibit large specific surface areas and flexible morphological changes. Furthermore, 2D materials with different compositions possess unique properties, such as the surface functional groups of graphene oxide and the lone pair electrons of black phosphorus. Due to different properties, these materials have different *in vivo* fates when administered to physiological environments. In this section, we introduce several classes of 2D materials with broad biomedical applications. First, graphene derivatives and other monoelemental 2D materials (Xenes) are discussed. Then, MXenes with multi-element components are introduced. Finally, TMDs, a class of multi-element 2D materials with complex crystal phases, are reviewed. Although some properties have not been fully explored, we believe that these 2D materials have exhibited unique advantages in biological applications.

3.1 Graphene derivatives

Graphene and its derivatives have attracted widespread attention in the field of biomedicine owing to their attractive drug loading capacity and sensitive external stimulation response. However, their long-term fate *in vivo* remains a concern when faced with the clinical translation of these materials. Fluorescence imaging is one of the most commonly used methods to track GO's behavior *in vivo*. However, the intrinsic limitations of fluorescence imaging, including non-quantitative results and background fluorescence, significantly limit the accuracy of this method. To solve this problem, Yang *et al.*[1] used a radiolabeling method to monitor the pharmacokinetics and long-term biodistribution of PEGylated small-size GO (10–30 nm), as shown in Fig. 6B–F. As a prerequisite of effective tracking, ^{125}I-labeled GO exhibited stable radiolabeling in mouse plasma at 37 °C for over 15 days. The pharmacokinetics of GO followed the two-compartment model, which divides the

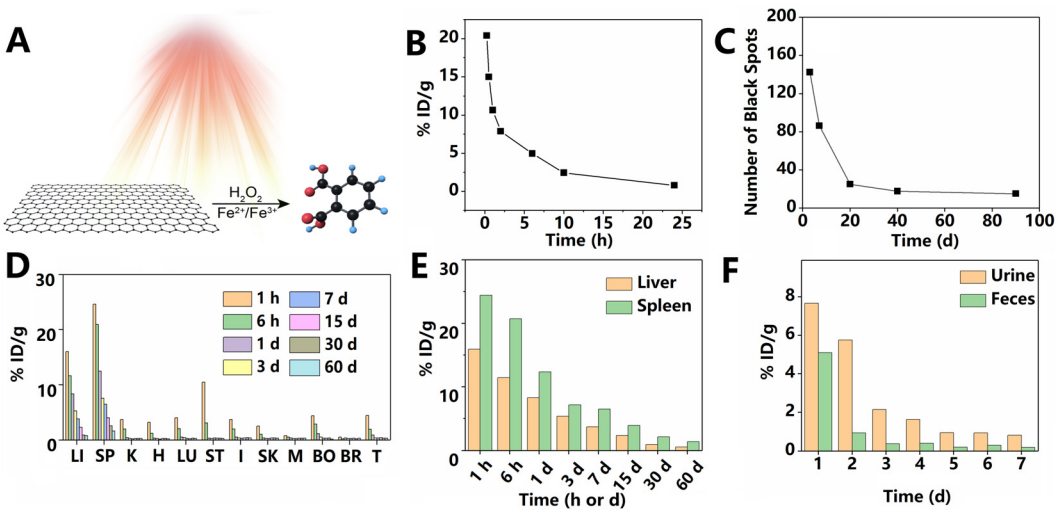

Fig. 6 (A) GO degradation mechanism based on the photo-Fenton reaction. Degradation products may be oxidized polycyclic aromatic hydrocarbons. Adapted and modified with permission from ref. 39 Copyright (2014) American Chemical Society. (B) Blood circulation curve of GO. (C) Number of black spots found in liver sections at different time points PI with GO. Black spots represent the accumulated GO. (D) Time-dependent biodistribution of GO. LI: liver; SP: spleen; K: kidney; H: heart; LU: lungs; ST: stomach; I: intestine; SK: skin; M: muscle; BO: bone; BR: brain; and T: thyroid. (E) GO signal in the liver and spleen at different time points PI. (F) GO signal in urine and feces at different time points PI. Adapted and modified with permission from ref. 1 Copyright (2011) American Chemical Society.

body into two parts: the central compartment with fast material exchange (*e.g.*, blood, heart, and liver) and the peripheral compartment with slow material exchange (*e.g.*, muscle, bone, and fat).[38] According to the two-compartment model, the blood circulation of GO was divided into a rapidly distributed component and a significantly slower elimination component: the half-lives of the blood circulation in the first and second phases were 0.39 ± 0.097 and 6.97 ± 0.62 h, respectively. At 1 h PI, GO was distributed across different organs of the mice. Strong signals were observed in the bone at the early time points PI, which may be due to macrophage uptake of GO into the bone marrow. Similar to other nanomaterials, the radiation signal was mainly concentrated in the MPS, such as the liver and spleen. Combining the results of tissue sections and gamma counters, researchers found that GO in the liver significantly decreased over time. This may be attributed to the enzymatic and photo-Fenton degradation of graphene, as reported in previous studies (Fig. 6A).[39] However, a small amount of GO can still be detected in the liver after 20 days. This study also found that GO accumulated in the kidneys and intestine, indicating possible excretion, which was confirmed by the high radioactivity in the feces and urine of the experimental animals. This study indicates that GO nanosheets are distributed throughout the body after administration and retained in the spleen for a long time. The concern about the long-term toxicity of GO nanosheets is thus reasonable.

A similar animal study was performed using a direct bladder puncture method. Approximately 50–60% of GO were excreted in the urine 2 h after injection.[7] Neither significant changes in kidney function nor structural damage to the glomerular and tubular regions was found after injection of well-dispersed GO nanosheets. Even when exposed to a dose that was significantly higher than the therapeutic one, the endothelial and podocyte cell cultures could regain their barrier function. Notably, although the size of most GO nanosheets is larger than the pore size in the kidneys, numerous studies demonstrated that GO could pass through these pores by rolling, crumpling, or folding, as shown in Fig. 7.[7] Consequently, thin graphene with high mechanical flexibility is easily discharged from the body. Although most GO nanosheets are excreted in the urine, a small but significant part remains isolated in the spleen (~1.6% ID g^{-1} at 60 days after i.v. injection).[1] After injection, GO was found to accumulate in the marginal zone macrophages of the spleen of the mouse.[6] Although the quantity of GO nanosheets in the spleen decreases rapidly over time, a small amount could only be removed from the body by slow degradation, and this process took over 270 days.[6] Compared to the first day PI, the mouse spleen showed an increased Raman peak corresponding to the GO defect on the seventh day, which corresponds to the first stage of the amorphous trajectory of carbon. Throughout the amorphous trajectory, the structure of GO would transform from a sp^2-hybridized carbon structure to a mainly tetrahedral sp^3 amorphous carbon phase. While in the first stage, the GO components accumulate defects and the size of the internal sp^2-hybridized crystal domain decreases, from the 7th to the 14th day, the defect signal increased slowly, which may be attributed to the presence of initially degraded debris' physisorption on the surface of GO. This debris protected the GO nanosheets and extended the time required for biodegradation. Subsequently, the spleen-residing GO entered the second stage, at which a large number of amorphous carbon structures were produced. At 270 days after injection, the characteristic Raman peak of GO was almost undetectable, indicating that most of GO was degraded. Over time, the GO in the spleen cells also showed a changed morphology under TEM with more defects and weaker electron diffraction intensity. It was speculated that GO within the spleen would slowly accumulate defects, eventually leading to a complete loss of the planar structure. Notably, the GO nanosheets incubated *in vitro* without light at 37 °C did not show similar structural changes, indicating that the physiological environment of the spleen played a key role in the GO degradation process. The above studies showed that the degradation process of GO in the body lasts over a duration of 270 days. Such a comprehensive study of the biodistribution and clearance of GO in the body is essential to assess its long-term potential toxicity.

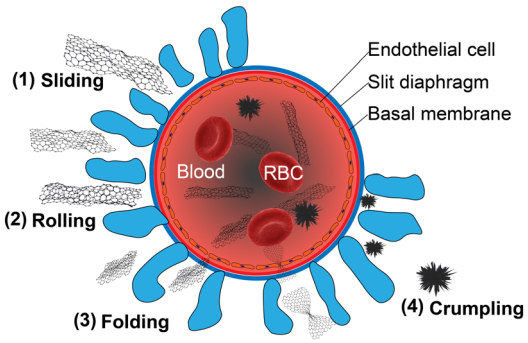

Fig. 7 Schematic diagram of GO nanosheets passing through the glomerular filtration barrier. During this process, morphological reconfiguration of nanosheets may happen, including sliding, squeezing, rolling, or folding. Adapted and modified with permission from ref. 7 Copyright (2016) American Chemical Society.

Although numerous studies have been conducted on the *in vivo* behavior of graphene, a label-free and quantitative method to detect graphene is in great demand. In 2015, Chen *et al.*[40] used mass spectrometry imaging to show the distribution of GO *in vivo* with a sensitivity of 0.04 μg mL^{-1} and compared it with carbon nanotubes and carbon nanodots. Carbon nanomaterials including carbon tubes, carbon dots, and GO produced anionic carbon clusters under ultraviolet laser irradiation in the mass spectrometer. These anionic carbon clusters, including C_2^-, C_3^-, C_4^-, C_5^-, C_6^-, C_7^-, C_8^-, C_9^-, and C_{10}^-, could be used as a fingerprint to distinguish carbon nanomaterials from tissues. Compared with carbon tubes and carbon dots, GO accumulated less in kidney tissues due to high GO concentrations in the lungs. Using this novel detection method, researchers expect to obtain a deeper understanding of the *in vivo* fate of 2D materials.

In addition to GO, the behavior of rGO *in vivo* likewise received significant attention from researchers in recent years. Syama *et al.*[41] used Raman spectroscopy to study the distribution and metabolism of rGO administered intraperitoneally and intravenously. rGO was widely distributed in major organs such

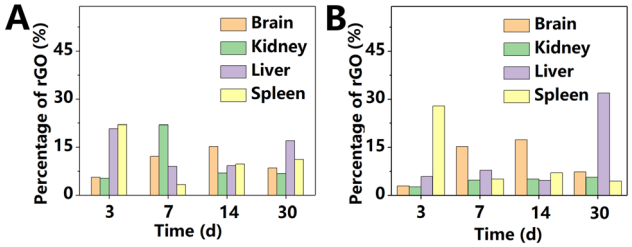

Fig. 8 Percentage of rGO in the Raman chemical map of different tissues in mice, injected intravenously (A) or intraperitoneally (B). Adapted and modified with permission from ref. 41 Copyright (2017) Elsevier.

as brain, liver, kidneys, spleen, and bone marrow following injection. In both injection methods, the signal of rGO in the blood reached the maximum at 3 h PI, and became very weak after 7 days. After i.v. and intraperitoneal injection, rGO was effectively absorbed from the systemic circulation and was phagocytosed by the macrophages present in the MPS. In contrast to the rapid systemic distribution after i.v. injection, the nanoparticles administered intraperitoneally were gradually absorbed from the abdominal cavity, and then slowly transferred to various organs, as shown in Fig. 8. Furthermore, after intraperitoneal injection, long-term retention of rGO was found in the abdominal cavity. Notably, unlike other studies on GO, in this study, the experimental results showed that only a small amount of rGO was excreted through urine. The biliary system may be the main excretion route of rGO. Due to the long-term retention of rGO *in vivo*, it is necessary to carefully evaluate the side effects of rGO before clinical application.

3.2 Monoelemental materials (Xenes)

As a relatively novel category in the 2D materials family, Xenes have been developing rapidly in recent years. The simple element composition is accompanied by a simple metabolism and degradation mechanism, which is highly promising to clinical applications. Different elemental compositions endow Xenes with unique biological advantages. For example, phosphorus is an osteogenic element, and arsenic is suitable for the treatment of acute promyelocytic leukemia.[4,42] Most Xenes are believed to be biodegradable; however, the degradation mechanism is not understood to date. Generally, the biodistribution of Xenes is similar to that of other 2D materials. The liver, lungs, kidneys, and tumor sites are the most commonly accumulated sites *in vivo*. Compared with the well-studied graphene nanosheets, there is limited study on the long-term fate of Xenes *in vivo*. In this section, the latest research on the *in vivo* fate of different types of Xenes is introduced.

3.2.1 Black phosphorus. As a new star in the field of biomedicine, BP nanosheets have attracted significant attention owing to their excellent therapeutic efficacy and biodegradability. Wang *et al.*[3] prepared BP nanosheets and used them as a photosensitizer. Interestingly, this research revealed that BP nanosheets could be stored stably in deoxygenated water for 2 weeks in the dark. In sharp contrast, most BP nanosheets could be easily degraded within 2 weeks with exposure to 20 min irradiation every 2 days. The inductively coupled plasma-atomic emission spectrometry (ICP-AES) test showed that the degradation products of BP nanosheets were phosphite ions, phosphate ions, and other P_xO_y species, among which phosphite ions were the main product, as shown in Fig. 9D. Owing to the rapid biodegradation rate and biocompatible degradation products, BP nanosheets possess great potential for clinical translation. Tao *et al.*[43] studied the biodistribution of fluorescent PEGylated BP nanosheets by whole-animal near-infrared imaging. At 1 h PI, the BP nanosheets exhibited systemic distribution. At 12 h and 24 h PI, the overall fluorescence intensity of the mouse body was significantly weakened due to the clearance of BP nanosheets. Notably, the fluorescence signal in the tumor site gradually increased during 24 h, indicating the targeting capability of the BP nanosheets. This study also found that BP nanosheets showed significantly prolonged circulation compared with small-molecule drugs. Subsequently, a recent study showed that the blood circulation of BP nanosheets also followed a standard two-compartment model, similar to that of GO nanosheets.[44] However, the half-lives of the first and second stages of BP nanosheets were 1.3 and 125.7 min, respectively, significantly shorter than that of GO. After the tail vein injection, the fluorescently labeled BP nanosheets showed preferential accumulation in the kidneys, and reached a peak signal within 0.5 h. At 5 min after injection, the fluorescence intensity in the glomerulus began to decrease, which was related to the release of the fluorescent dyes caused by the collapse of the BP structure. Although the above work studied the biodistribution and metabolism of BP nanosheets *in vivo*, the intrinsic limitations of the optical-based imaging method make it difficult to quantitatively and accurately evaluate the biodistribution of BP nanosheets. To solve this problem, Hu *et al.*[45] used PET technology to track the *in vivo* behavior of ^{64}Cu labeled BP nanosheets. After modification with the cyclic peptide c, BP nanosheets exhibited excellent tumor targeting. The highest tumor uptake of BP nanosheets was $\sim$5.2% ID g^{-1} at 16 h PI. Even at 40 h after injection, $\sim$4.8% ID g^{-1} BP nanosheets remained, indicating the effective tumor accumulation of BP nanosheets. Similar to the results of PET, the tissue section data showed that the tumor uptake of BP nanosheets continued to increase from 0 to 24 h PI. In contrast, the BP nanosheets in the liver, spleen, and lungs decreased rapidly at 3 h PI, which may be attributed to the oxidation of the BP nanosheets by the oxygen which is present in a high level in these organs.[8] Notably, the signal of BP nanosheets in the blood increased over time from 1 to 42 h, which may be related to the reversible uptake of BP. The authors believed that the large-sized BP nanosheets would oxidize, degrade, reduce their size, and re-enter the blood circulation after being swallowed by the MPS-rich organs. The strong radioactive signals from the kidneys and urine indicated that BP nanosheets were likely to be excreted in urine.

Phosphate anions, the degradation product of BP, are abundantly present in the human body and are biocompatible. However, the sharp rise of cytosolic phosphate anions may cause some side effects, such as affecting cellular ATP hydrolysis and inducing programmed cell death. Interestingly, Zhou *et al.*[46] found that this toxicity could selectively target

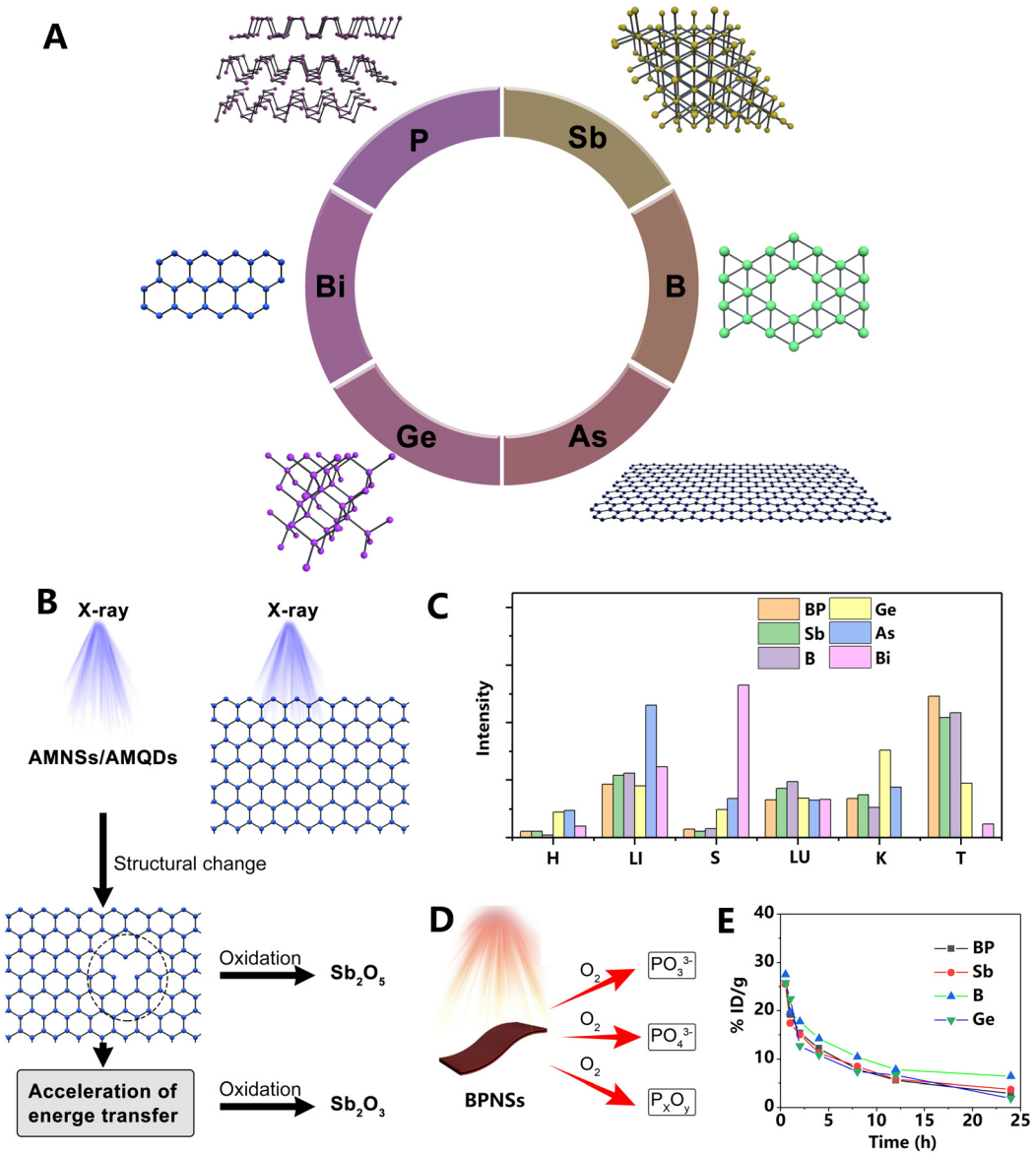

Fig. 9 (A) Structure of Xenes discussed in this section. (B) Schematic illustration of oxidation of Sb nanosheets under X-ray irradiation. Adapted and modified with permission from ref. 2 Copyright (2019) Wiley-VCH Verlag GmbH & Co. KGaA, Weinheim. (C) Biodistribution of various Xenes. To facilitate comparison of the relative tissue distribution of each material, the data were normalized. H: heart; LI: liver; S: spleen; LU: lungs; K: kidneys; and T: tumor. (D) Oxidation products of BP nanosheets. Irradiation can accelerate the oxidation process. (E) Blood circulation curve of various Xenes. Adapted and modified with permission from ref. 17, 42, 43, 51, 52 and 54 Copyright Wiley-VCH Verlag GmbH & Co. KGaA, Weinheim and Elsevier.

cancer cells, which exhibit significantly faster oxidative stress and energy metabolism compared to normal cells. Their results indicate that the sharply elevated phosphate anions induced cancer cell G2/M phase arrest, subsequent apoptosis, and autophagy-mediated cell death. The IC_{50} values of BP nanosheets on cancer cells were as low as 2 $\mu g\,mL^{-1}$, while normal cells showed over 80% survival rate under treatment with a higher concentration of BP (4 $\mu g\,mL^{-1}$). Very recently, another excellent study also observed the selective killing of cancer cells by BP nanosheets themselves.[47] In this study, BP nanosheets were found to fragment mitotic centrosomes by deactivating the centrosome kinase PLK1. Consequently, the mitotic progression of cancer cells was delayed, and eventually apoptosis occurred. Notably, a variety of phosphorus-based nanomaterials exhibited the mitotic block effect, while the degradation products of BP nanosheets did not show this performance. Despite the exciting results of these studies, their data are inconsistent with those of some others.[3,48] The biological effects of BP nanosheets are complex and can be affected by numerous factors, which may lead to inconsistencies. Further careful investigation of the interaction between BP and the biological milieu is necessary.

3.2.2 Antimony. Sb has been used to treat infectious parasitic diseases for centuries.[17] However, 2D Sb nanosheets did not gain attention in medicine until 2017. After the first successful preparation of 2D Sb nanosheets in 2016,[49] it was

found that Sb nanosheets exhibited numerous excellent properties, including good thermal conductivity, superior carrier mobility, and unique spintronic properties. Encouraged by the success of using BP nanosheets in biomedical applications, researchers studied the potential use of 2D Sb, which is a congener element of phosphorus. Tao *et al.*[17] used an improved liquid phase exfoliation to fabricate Sb nanosheets with an average size of ~90 nm and a thickness of ~6 nm. The Sb nanosheets exhibited effective photothermal conversion (41.8%), high drug loading capacity (150%), and drug release with a dual response to pH and NIR. At 2 h PI, part of the Sb nanosheets reached the subcutaneous tumor, which was observed by fluorescence imaging. The fluorescence signal of the Sb nanosheets at the tumor site gradually increased over time. Even after 24 h, the fluorescence intensity was still significantly higher than that of the surrounding normal tissues, indicating a good retention at the tumor site. In addition to tumors, the liver, spleen, kidneys, and lungs also showed significant material retention. The authors believed that the material enrichment in the liver and kidneys was related to the absorption of the MPS and metabolism of the kidneys. On the seventh day PI, significant Sb signal could still be detected in the liver, spleen, kidneys, and lungs by ICP-MS. By the 30th day PI, the level of Sb in major organs decreased to a negligible level. To assess potential long-term toxicity, the biodegradability of Sb nanosheets was investigated. The photothermal performance of Sb nanosheet aqueous solution was found to attenuate rapidly under irradiation. This result demonstrated that the degradation rate of Sb nanosheets may be faster than that of BP nanosheets, which are known for their biodegradability. On the contrary, in ethanol solution or deoxygenated water, Sb nanosheets exhibited negligible degradation, indicating that water and oxygen play an important role in the degradation of Sb nanosheets. Notably, among the two main oxidation states of Sb, Sb(III) is significantly more toxic than Sb(V), such that it is necessary to further determine the degradation products of Sb nanosheets. To this end, Duo *et al.*[2] designed PLGA-coated Sb nanosheets with controllable valence states as a radiotherapy sensitizer. They found that the zero-valent Sb (Sb(0)) on the surface was easily oxidized to Sb(V), but it could be avoided by modification. After storage in fetal bovine serum for 13 days and 55 days, the normalized absorption intensity of the PLGA-modified material retained 88% and 70%, respectively. This phenomenon indicated that this modification strategy significantly improves the stability of Sb nanosheets. Interestingly, X-rays could induce the conversion of Sb(0) to Sb(III), which was almost undetectable in the non-irradiated group. At 19 days PI, most of the Sb element was concentrated at the tumor site instead of normal organs, which was supported by the results of ICP-MS. These results indicate the potential of Sb nanosheets as a biodegradable therapeutic material in the biological field.

3.2.3 Boron. Because of the trivalent electronic configuration, boron (B) nanosheets exhibit polymorphism, which distinguishes them from other 2D materials. B has been clinically used in boron neutron capture therapy, as the reaction range of ionized ^{10}B is close to the size of cancer cells.[50] After being exfoliated into ultra-thin nanosheets, B exhibits greater performance in biomedical applications. In 2018, Ji *et al.*[51] combined liquid phase exfoliation and thermal oxidation etching to obtain high-quality B nanosheets for cancer treatment. The prepared B nanosheets have a planar size of ~100 nm and an ultrathin thickness (<5 nm). The excellent photothermal conversion efficiency (42.5%) and high drug loading capacity (114%) indicate the great application potential in biomedicine. After being coated with PEG, the B nanosheets remained stable in water for over 30 days. Compared with the anti-cancer drug doxorubicin (DOX), B nanosheets showed prolonged circulation time in pharmacokinetic experiments. The results of both fluorescence imaging and PA imaging showed that the material could be effectively accumulated in the tumor site at 24 h after i.v. injection. Among major organs, the most of material fluorescence signals were detected in the liver, lungs, and kidneys. The excellent performance and tumor-specific biodistribution are favorable for the application of B nanosheets in the biological field, but its clearance *in vivo* must be carefully studied.

3.2.4 Germanium. As an essential trace element for the human body, the amount of germanium (Ge) that the human can uptake safely from food is as high as 367–3700 μg every day.[52,53] Considering the high biocompatibility of Ge, a team recently synthesized ultra-small Ge QDs and used them as photothermal agents.[53] To improve the stability and dispersion in the physiological environment, the surface of Ge QDs was coated with PEG through hydrophobic interaction and van der Waals force. After modification, Ge QDs exhibited strong broadband optical absorption, extremely high photothermal conversion efficiency, photothermal stability, and biocompatibility. At 24 h PI, the accumulation of Ge QDs in the tumor site reached their maximum, with approximately 15% of the signal being concentrated in the tumor. Comparing main organs and tumors, most of the Ge QDs were detected in the kidney at 24 h PI, indicating rapid metabolism. Subsequently, the same group used liquid phase exfoliation to fabricate Ge nanosheets with a size of ~60 nm and a thickness of ~5 nm.[52] The Ge nanosheets began to accumulate at the tumor site at 4 h after tail vein injection. Unlike Ge QDs, the signal intensity of the Ge nanosheets at the tumor site was weakened at 8–24 h PI. Evident material signals were observed in the spleen, liver, kidneys, and lungs 8 h after treatment, indicating possible renal excretion and liver metabolism. The results of fluorescence imaging and PA imaging also proved the above conclusions. This result indicates that the Ge nanosheets can be efficiently cleared after therapy. However, more long-term and quantitative studies are needed to investigate the *in vivo* fate of Ge nanosheets before clinical application.

3.2.5 Arsenic. Arsenic-containing agents have been used as traditional medicines in the treatment of various diseases such as psoriasis, syphilis, and rheumatism for more than 2000 years. Currently, arsenic-based drugs are also widely used in the treatment of cancer, especially acute promyelocytic leukemia (APL).[42] Encouraged by the tremendous progress of arsenic (As) agents, researchers used the liquid phase exfoliation method to prepare As nanosheets with a size of 200.8 nm and explored their performance in APL treatment.[42]

After 10 days of storage in dimethyl sulfoxide (DMSO), the Raman spectrum of As nanosheets did not change significantly, indicating the good stability of As nanosheets in DMSO. The *in vitro* experiments showed that the As nanosheets exhibited selective toxicity. In total, 1.2 μg mL^{-1} As nanosheets could inhibit over 80% APL NB4 cells, while those of the same concentration did not significantly inhibit the growth of normal human liver cells. In NB4 cells, As nanosheets may be oxidized to As_2O_3. Furthermore, As nanosheets produced a large amount of ROS in NB4 cells, which induced cell apoptosis. At 24 h after being injected into the mice, most As nanosheets were detected in the liver and kidneys. Although As nanosheets show great potential in APL treatment, the *in vivo* behavior of As nanosheets must be further investigated due to toxicity concerns.

3.2.6 Bismuth. Bismuth (Bi) is a non-toxic heavy metal element. Bi-containing agents have numerous impressive applications in biomedicine as radio- or photo-sensitizers. However, compared with graphene and BP, it is more difficult to exfoliate Bi with a honeycomb lattice puckered layered structure. Wang *et al.*[54] combined the freeze-thaw process mediated by water molecules, and the reduction process triggered by sodium borohydride to prepare Bi–Bi_2O_3 heterojunction nanosheets with a size of ~200 nm and a thickness of ~14 nm. Coated with bovine serum albumin, Bi nanosheets exhibited an extinction coefficient of 6.4 L g^{-1} cm^{-1}, a photothermal conversion efficiency of 19.4%, and a strong ROS generation ability. More importantly, *in vivo* experiments showed that Bi nanosheets could reach the maximum tumor uptake of 4.13 ± 0.10% within 4 h, supported by data from ICP-MS and PA imaging. In addition, 34% of the modified Bi nanosheets degraded within 18 h in a simulated physiological environment, implying that long-term toxicity may be avoided.

3.3 MXenes

MXenes are a 2D material family that is composed of transition metal carbides, nitrides or carbonitrides, and it contains more than 70 members. Usually, MXenes are prepared by selective etching using their precursor MAX, where M, A, and X are early transition metals, elements of group IIIA or IVA and C or N, as shown in Fig. 10A.[60] The MXenes that are prepared in this way often have functional groups on their surface, which is conducive to surface modification and drug loading.

As the first prepared MXene, titanium carbide (Ti_3C_2) has been applied to various fields, including biomedicine. Because of the strong absorption in NIR, Ti_3C_2 nanosheets are a potential photothermal agent. However, the size of Ti_3C_2 nanosheets obtained by traditional methods is relatively large, which is not suitable for biological applications. To solve this problem, Lin *et al.*[55] prolonged the HF etching time to prepare Ti_3C_2 nanosheets with a size of ~150 nm. After sealing, Ti_3C_2 nanosheets could be uniformly dispersed in water for several weeks, indicating good dispersibility and stability. Ti_3C_2 nanosheets exhibited excellent photothermal stability under five laser on/off cycles. The blood circulation half-life of Ti_3C_2 nanosheets was ~0.76 h, as shown in Fig. 10C. At 24 h PI, Ti_3C_2

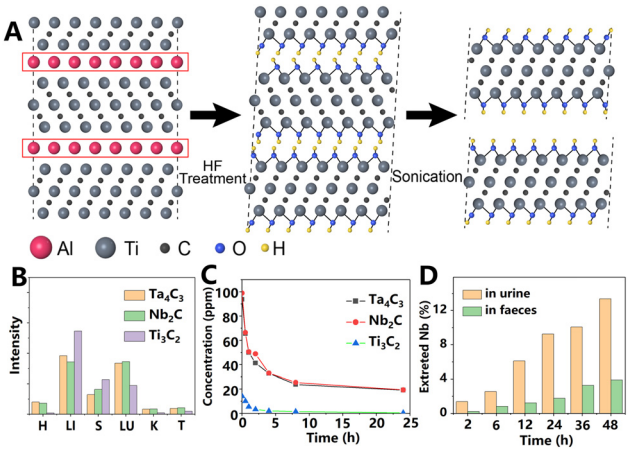

Fig. 10 (A) Schematic of MXene exfoliation (Ti_3C_2) by selective etching and sonication. During this process, Al atoms in the precursor are replaced by OH in HF. Subsequently, dispersed nanosheets were obtained by sonication. Adapted and modified with permission from ref. 60 Copyright (2011) Wiley-VCH Verlag GmbH & Co. KGaA, Weinheim. (B) Biodistribution of various MXenes. To facilitate comparison of the relative tissue distribution of each material, the data were normalized. H: heart; LI: liver; S: spleen; LU: lungs; K: kidneys; and T: tumor. (C) Blood circulation curve of various MXenes. (D) Nb signal in urine and feces at different time points PI of Nb_2C. Adapted and modified with permission from ref. 55 and 56 Copyright (2017) American Chemical Society and ref. 59 (2018) Wiley-VCH Verlag GmbH & Co. KGaA, Weinheim.

nanosheets were mainly distributed in the liver, spleen, and lungs, as shown in Fig. 10B. The accumulation of Ti_3C_2 nanosheets in the kidneys was much less than other 2D materials, such as BP, As, and Ge nanosheets.

Compared with Ti_3C_2 nanosheets, MXene-niobium carbide (Nb_2C) nanosheets have better performance in biodegradation and metabolism.[56] After being dispersed in water for several months, researchers obtained evidence of surface oxidation of Nb_2C nanosheets through TEM observation. When H_2O_2 was present, the nanosheets lost their planar structure within 24 h. In a simulated human environment with human myeloperoxidase and H_2O_2, Nb_2C nanosheets almost completely degraded within 24 h. *In vivo* experiments showed that within 2 days after i.v. injection, 20% of Nb would be excreted from mice through urine and feces. Among the main organs, the liver, spleen, and lungs accumulated the most Nb. Notably, the decline in Nb content in the lungs was significantly slower than that in other major organs. The passive accumulation efficiency of Nb element in the tumor site reached a peak of 2.24% ID g^{-1} at 24 h after injection, and the blood half-life was about 1.31 h. Subsequently, the same research group found that Nb_2C nanosheets could protect the body from the damaging effects of ionizing radiation by scavenging free radicals.[57] Nb_2C nanosheets with an average size of 150 nm, a thickness of ~0.5–1 nm, and a specific surface area of 2.997 m^2 g^{-1} were prepared by selective etching assisted liquid phase exfoliation. In both *in vitro* and *in vivo* experiments, Nb_2C nanosheets showed evident protective effects on irradiated cells and animals. After injection, the nanosheets distributed in almost all tissues including liver, lungs, spleen, heart, kidneys, testis, and small intestine, which was conducive to comprehensive

protection. Compared with the previous study, the Nb_2C nanosheets in this article exhibited a significantly prolonged plasma half-life (3.8 h). Notably, at 4–48 h PI, the liver showed the most evident uptake and clearance of Nb_2C nanosheets, indicating possible liver metabolism pathways, including liver metabolism and bile excretion. At 24 h PI, the accumulation of modified Nb_2C nanosheets in the organs reached the maximum, while in the previous study, the Nb element concentration in the organs had been decreasing at this time point. The different results of the two pieces of work may be due to the different animal models used: the previous study used immunodeficient nude mice, while this work used normal mice. Similar to the previous study, 20% Nb was excreted in urine and feces within 48 h after injection, as shown in Fig. 10D. Nearly 80% Nb was excreted in feces (57%) and urine (23%) within 7 days after injection, which avoids potential long-term toxicity.

In addition to Ti_3C_2 and Nb_2C, tantalum carbide (Ta_4C_3) nanosheets showed unique advantages.[58] The biocompatible Ta element with a high atomic number (Z = 73) makes Ta_4C_3 nanosheets a promising CT contrast agent. Similar to Ti_3C_2, Ta_4C_3 nanosheets remained stable in water for several weeks.[59] The PA and CT signals of Ta_4C_3 nanosheets at the tumor site increased continuously within 24 h after injection. The maximum passive accumulation efficiency of the nanosheets was 1.41%, and the half-life was ~1.59 h. The enrichment of Ta_4C_3 nanosheets in the main organs of mice occurred in liver, lungs, spleen, heart, and kidneys, in that order. Compared with Nb_2C, there is still work to be done before clinical application to understand the degradation and metabolism of Ta_4C_3 nanosheets.

3.4 Transition metal dichalcogenides

Transition metal dichalcogenides (TMDs) can be expressed as MX_2, where M is a transition metal, and X is a chalcogen (S, Se, or Te). Compared with other 2D materials, the properties of TMDs are more diverse. TMDs show different phases with the change of the link mode of the two elements, or the stacking way between layers. In addition, the band gap of some TMD nanosheets change from indirect to direct with the decrease in layers. The unique properties have attracted extensive attention from researchers, and a variety of applications based on TMDs have been developed, including biomedicine. Recently, Yim *et al.*[61] used TMDs as antioxidants to treat sepsis. Molybdenum disulfide (MoS_2), tungsten dichalcogenides (WS_2), and tungsten selenide (WSe_2) nanosheets with similar size and thickness were fabricated by liquid phase exfoliation. After being stored in an aqueous solution for 14 days, the characteristic absorption peaks of the three PEG-modified TMD nanosheets did not change significantly, indicating great stability. Owing to their optimal ROS and reactive nitrogen species clearance effect, WS_2 was used on a septicemia mice model. At 3 h PI, the liver, spleen, lungs, and kidneys indicated evident material signals, as shown in Fig. 11A. At 3 days PI, no fluorescence signal of the nanosheets was observed in the above-mentioned four organs. The rapid clearance of WS_2 nanosheets reduced the risk of long-term toxicity. Compared with i.v. injection, the intraperitoneal injection of nanosheets led to faster distribution in major organs

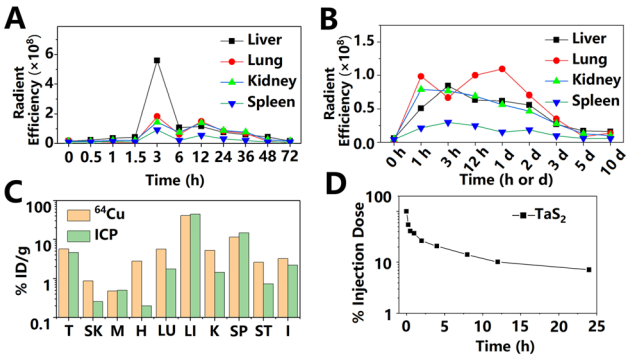

Fig. 11 Biodistribution of WS_2 nanosheets at different time points after i.v. (A) or intraperitoneal (B) administration. Adapted and modified with permission from ref. 61 Copyright (2020) American Chemical Society. (C) Biodistribution of MoS_2 nanosheets at 24 h after i.v. injection, measured by radioactivity or ICP-AES. The data indicate the great impact of test methods on the biodistribution results. Adapted and modified with permission from ref. 62 Copyright (2015) American Chemical Society. (D) The pharmacokinetics of TaS_2 nanosheets. Adapted and modified with permission from ref.65 Copyright (2017) Wiley-VCH Verlag GmbH & Co. KGaA, Weinheim.

within 1 h, as shown in Fig. 11B. However, until the 10th day, a small amount of material signals could still be detected in the liver and lungs, demonstrating that intraperitoneal injection led to a longer retention time of the nanosheets than i.v. injection.

Compared with graphene and BP, metal modification of MoS_2 is simpler due to the presence of the sulfur element. To fabricate MRI and PET contrast agents, Liu *et al.*[62] modified the iron oxide particles and ^{64}Cu on MoS_2 nanosheets through sulfur chemistry and the affinity of sulfur–Cu^{2+}, respectively. The as-prepared MoS_2 nanosheets and iron oxide particles were further modified with lipoic acid PEG and amino-terminated six-arm PEG, which significantly improved the blood circulation time. In T_2-weighted MR images, tumors, liver, and kidneys showed significantly reduced MR intensity at after 8 h PI, signaling MoS_2 enrichment in these tissues. In contrast, the MR intensity of muscle did not decrease, which was related to less MoS_2 nanosheet enrichment. The PET test also provided similar results. At 3 h PI, there was a significant ^{64}Cu-labeled MoS_2 nanosheet signal at the tumor site. At 24 h, the accumulation of MoS_2 nanosheets in the tumor reached a maximum of over 5% ID g^{-1}, while the material accumulation of muscle tissue was consistently below 1% ID g^{-1} within 1 day PI, as shown in Fig. 11C. The enrichment at tumor sites facilitates the application of MoS_2 nanosheets as a drug delivery platform.

Although PET yields credible results of *in vivo* distribution, its safety and half-life dependent detection time limit its clinical application. In recent years, Xue *et al.*[63] developed a label-free laser desorption/ionization mass spectrometry imaging (LDI MSI) strategy and used it to quantitatively evaluate the tissue distribution and drug release of MoS_2 with sub-organ high resolution. The results showed that pure MoS_2 nanosheets were enriched in the lungs within 1 h PI, while the material signals were almost undetectable in the heart, kidneys, and brain, demonstrated by LDI MSI at the same time. At 1 and 2 days PI,

the signal intensity in the spleen and liver increased significantly, while that in the kidneys, heart, and brain remained almost undetectable. Considering the large size of the MoS_2 nanosheets used in this article (750 ± 230 nm), it was difficult for the material to be cleared through glomerular filtration or penetrate the blood vessel barriers of the heart and brain. At 30 days PI, there was still a small quantity of MoS_2 nanosheets in the MPS, which indicated the long-term accumulation of MoS_2 nanosheets in the body. Similar to carbon materials, the MoS_2 nanosheets in the spleen were mainly concentrated in the red pulp area. After encapsulating with PEG, MoS_2 nanosheets showed faster organ metabolism, which is consistent with previous studies. At 2 days after the injection, PEG–MoS_2 nanosheets could hardly be detected in the lungs, kidneys, heart, and brain tissues. Subsequently, the authors injected MoS_2 nanosheets into a murine H22 orthotopic tumor model. The signal of MoS_2 nanosheets in normal liver tissues was about 3.5 times higher than that of tumor foci, indicating that the enrichment of MoS_2 nanosheets in normal liver tissues was much higher than that in liver cancer tissues. The fluorescence imaging employed in most studies failed to obtain sub-organ level results. This study suggests that we are far from fully understanding the *in vivo* behavior of 2D materials.

Tantalum (Ta) has been used as clinical implants, artificial joints, stents, and vascular clips for more than 50 years.[64] Therefore, Ta-derived nanomaterials may have potential in biomedical application. Liu *et al.*[65] used the liquid phase exfoliation method to fabricate TaS_2 nanosheets with a size of about 110 nm for a light-controlled drug delivery platform. Compared with DOX, the drug delivery platform based on TaS_2 exhibited a significantly prolonged blood circulation time, as shown in Fig. 11D. At 2 h PI, the CT signals of TaS_2 nanosheets were observed in the mouse heart. At 24 h PI, the tumor site of the mouse showed the strongest DOX fluorescence signal. The TaS_2 nanosheets distributed in the main organs of the whole body, with the liver and kidneys accumulating the most. Notably, NIR-treated tumors showed a stronger DOX fluorescence signal than the control group, which may be attributed to the accelerated release of DOX and the increased permeability in the tumor vascular system induced by heating.

Hao *et al.*[66] compared the long-term *in vivo* behavior of MoS_2, WS_2, and titanium disulfide (TiS_2), and the results are presented in Fig. 12. After PEG modification, MoS_2, WS_2, and TiS_2 exhibited hydrodynamic diameters of approximately 91, 72, and 102 nm, respectively. At 1 day PI, these nanosheets exhibited similar accumulation in MPS-rich organs (liver and spleen) due to the phagocytosis of liver Kupffer cells and spleen macrophages. The difference was that MoS_2 exhibited a significantly faster metabolic rate over time compared to WS_2 and TiS_2. The MoS_2 content *in vivo* was decreased sharply within 1 month after administration. High concentrations of Mo were detected in the urine and feces, suggesting that MoS_2 is excreted by the kidneys and gut. Unexpectedly, element W in

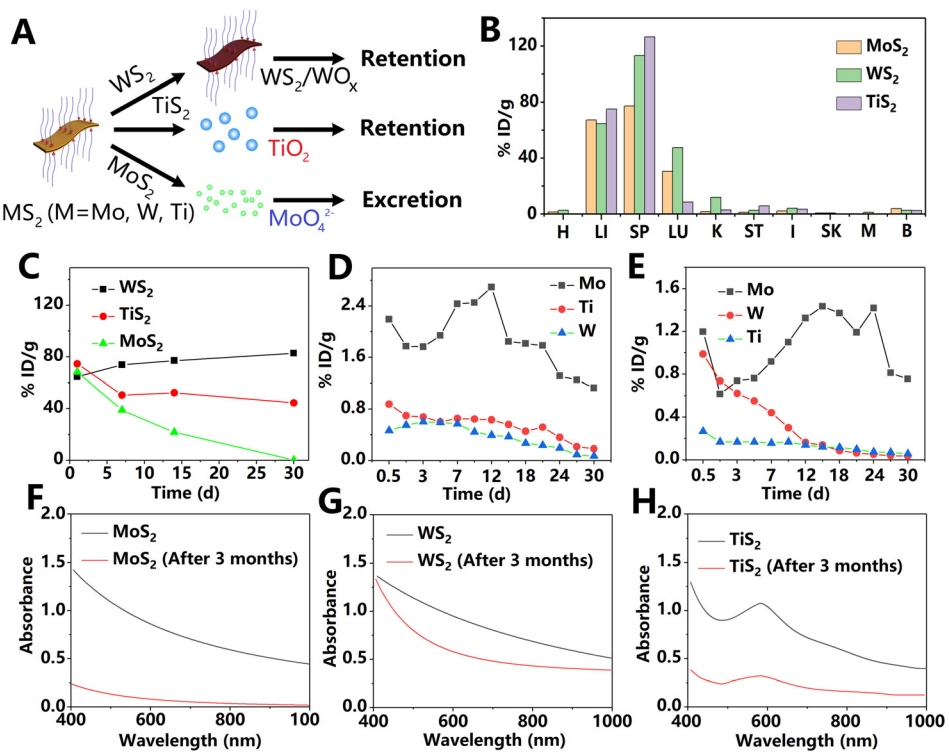

Fig. 12 (A) Schematic illustration of different clearance approaches of MS_2 nanosheets (M = Mo, W, and Ti). (B) Biodistribution of various TMDs. H: heart; LI: liver; SP: spleen; LU: lungs; K: kidneys; ST: stomach; I: intestine; SK: skin; M: muscle; and B: bone; (C) clearance effect of liver at different time points post i.v. injection of various TMDs. (D and E) Various TMD signals in urine (D) and feces (E) at different time points post i.v. injection. Absorption spectra of MoS_2 (F), WS_2 (G), and TiS_2 (H) before and after standing in PBS solution for 3 months. Adapted and modified with permission from ref. 66 Copyright (2017) Wiley-VCH Verlag GmbH & Co. KGaA, Weinheim.

the liver of WS_2-treated mice increased slightly over time, possibly because the transfer of WS_2 from the spleen to the liver is faster than liver excretion. The concentrations of W or Ti found in urine and feces of mice treated with WS_2 or TS_2 were significantly lower than Mo concentrations of the MoS_2-treated group, indicating the longer retention of WS_2 and TS_2 *in vivo*. Further experiments showed that, in PBS at room temperature, MoS_2, TiS_2, and WS_2 undergo degradation that is almost complete, evident degradation, and slight, respectively, within 3 months. Most degradation products of MoS_2 were water-soluble high-valence states Mo(VI) oxide. Unlike MoS_2, under the same conditions, WS_2 samples were incompletely oxidized into W(IV)/W(VI) compounds, while TiS_2 formed an insoluble white precipitate TiO_2 after oxidation. Furthermore, aggregates were observed in the degradation products of WS_2 and TiS_2, but not in the MoS_2 sample.

4. Discussion and future prospects

4.1 Research progress

In the past few decades, thousands of peer-reviewed papers have been published in the field of nanomedicine, and vast funds have been invested in related research. Nevertheless, there are very few clinically transformed nanomedicines, especially inorganic ones. The main reason for this situation involves the concerns about the potential long-term toxicity of inorganic nanomaterials. Considering the massive uptake of nanomaterials by MPS and clinical side effects, this concern is justified. In fact, among the most successful inorganic nanomaterials, some clinically approved iron oxide nanoparticles have been discontinued for safety reasons.[67] Today, 2D materials show attractive prospects in the field of nanomedicine. However, it is still too early for the clinical application of 2D materials. In addition to therapeutic efficacy, the biodistribution, degradation, and metabolism of 2D materials are most important factors to be considered and their careful evaluation is necessary before clinical transformation. Fortunately, researchers have become increasingly aware of the interaction between 2D materials and the physiological environment. Meanwhile, a variety of tracking methods have been developed to investigate the *in vivo* fate of 2D materials. These methods can be divided into *in vivo* and *in vitro* tracking methods. *In vivo* tracking methods include labeling methods and label-free methods. Due to its simplicity and safety, fluorescent labeling is one of the most popular methods for tracking the *in vivo* distribution of 2D materials. However, accompanied by strong background interference, this method is a semi-quantitative tool. In recent years, this technology has made great progress in the near-infrared second region, and is expected to obtain high quality images with a weak background signal. Compared with fluorescent labeling, although the radionuclide labeling method provides more accurate results, it has limitations in half-life and safety. These labeling methods can provide real-time and high-resolution results, but they require a time-consuming labeling process and suffer from the risk of label peeling, which can be avoided by label-free methods. As clinical imaging techniques, CT imaging and MRI were used to observe the *in vivo* behavior of nanosheets. To obtain high-contrast results, CT imaging is suitable for nanosheets containing high atomic number elements, while MRI was reported mainly in iron- and manganese-based nanosheets. In the work of photothermal therapy of 2D materials, photoacoustic imaging and photothermal imaging were widely used to demonstrate the biodistribution of materials, because the principle of these methods is the photothermal effect of materials. In addition to *in vivo* tracking, some methods were also used in tracking 2D materials *in vitro*, including ICP, transmission electron microscopy (TEM), Raman imaging and mass spectrometry imaging. ICP is one of the most popular elemental detection methods and is widely used in pharmacokinetic analysis. This method is highly accurate and suitable for most materials. TEM can provide images with nanometer-scale resolution, which has an irreplaceable advantage in observing the entry of nanosheets into cells or through biological barriers. In the study of the long-term fate of 2D materials, Raman spectroscopy has unique advantages. It can not only be used to determine the biodistribution but also to give information on the degradation of 2D materials. Mass spectrometry imaging is a novel technique, which has been used to analyze the biodistribution of 2D materials since 2015. Its unique advantage is that it can track nanosheets and loaded drugs simultaneously without labeling, which is of great significance for the study of drug delivery and release based on 2D materials. Overall, each of these methods has its own advantages and disadvantages, and therefore combining multiple tracking techniques is necessary to obtain comprehensive information on the *in vivo* behavior of 2D materials. With sufficient exploration, a variety of factors have been shown to have an impact on the *in vivo* behavior of 2D materials. Rational design of 2D materials can reduce the potential risk of off-target effects and long-term retention. 2D materials with actively changing size not only show increased accumulation in lesions but also good clearance and safety. Reasonable modification can change the surface potential, enhance blood compatibility, and promote immune escape of materials. By isolating the 2D materials from oxygen, the degradation rate of the material being coated is controllable. Furthermore, after special modification, 2D materials possess active targeting capabilities and enhanced therapeutic effects. Because of the significant influence of material components on the *in vivo* behavior, the interaction of composite materials with the physiological environment is often different from that of a single material (Table 1). The change in the band structure and the performance synergy also equip multi-component materials with unique advantages over the single component. Unlike traditional drugs, 2D materials can respond to a variety of external stimuli, including magnetic fields, lasers, and ultrasound, to adjust their *in vivo* behaviors. These physical means can remotely control the permeability of the blood vessel and the degradation rate of material, realizing intelligent treatment.

After being administered *in vivo*, most 2D materials tend to accumulate in MPS-rich organs, such as the liver and spleen. Then, 2D materials would degrade and be removed from the body. Some 2D materials degrade very quickly, including most

Table 1 Biodegradation and biodistribution of 2D materials and the corresponding tracking methods and the influencing factors. Fast biodegradation means that over half of the material degrades within 1 month, otherwise it is defined as slow biodegradation

Material	Size and thickness	Modification strategy	Main accumulation in organs	Biodegradation	Tracking method
GO	Size: 10–30 nm Thickness: ~1 nm[1]	PEG[1], cyclic R10 peptide,[22] DNA,[30] MicroRNA,[68] boron doping,[69] liposomes[70]	Spleen, liver, stomach, lungs, kidneys[1]	Slow[1]	Radiolabeling,[1] TEM, confocal Raman mapping,[6] mass spectrometry imaging[40]
rGO[41]	Size: ~1 μm Thickness: 4–9 nm	PEG	Liver, spleen	Slow	Raman spectroscopy
Graphdiyne oxide[71]	Size: 120 ± 15 nm Thickness: ~1.7 nm	iRGD peptide	Liver, spleen	N.A.	FL imaging
BP	Size: ~120 nm Thickness: 1–2 nm[43]	PEG,[43] polydopamine,[18] PLGA,[12] exosomes,[13] polyoxometalates[14] TiL_4,[19] Cu[45]	Liver, kidneys, lung[43]	Fast[3]	FL imaging,[43] radiolabeling[45]
Sb	Size: ~140 nm Thickness: ~4 nm[17]	PEG[17]	Liver, lung, kidneys, spleen[17]	Fast[17]	FL imaging, PA imaging,[17] ICP[2]
B[51]	Size: ~100 nm Thickness: <5 nm	PEG	Liver, lungs, kidneys	Slow	FL imaging, PA imaging
Ge[52]	Size: ~60 nm Thickness: ~5 nm	PEG	Kidneys, liver, lungs	N.A.	FL imaging, PA imaging
As[42]	Size: ~200.8 nm Thickness: >50 nm	N.A.	Liver	N.A.	ICP
Bi[54]	Size: ~200 nm Thickness: ~14 nm	Bovine serum albumin	Liver, spleen, lungs	Fast	ICP, CT, PA imaging
Te[72]	Size: ~300 nm Thickness: ~10 nm	Glutathione	Liver, spleen, kidneys	Fast	ICP, PA imaging
Ti_3C_2[55]	Size: ~150 nm Thickness: ~0.6 nm	Soybean phospholipid	Liver, spleen, lungs	N.A.	ICP
Nb_2C[56]	Size: ~150 nm Thickness: 0.3–0.8 nm	Polyvinylpyrrolidone	Liver, spleen, lungs, heart	Fast	PA imaging, ICP, TEM
Ta_4C_3[59]	Size: ~100 nm Thickness: ~1 nm	Soybean phospholipid	Liver, lungs, spleen, Heart	N.A.	ICP, CT, PA imaging
Mo_2C[73]	Size: 143.8 nm Thickness: 2.2–9.0 nm	Polyvinyl alcohol	Liver, spleen, lungs	Fast	ICP
WS_2[61]	Size: ~246 nm Thickness: ~4 nm	PEG	i.v. injection: liver i.p. injection: liver, lungs, spleen	Slow	FL imaging
MoS_2	Size: ~91 nm[66]	PEG[66] glucose oxidase[21]	Liver, spleen[66]	Fast[66]	Radiolabeling,[62] ICP,[66] Mass spectrometry imaging[63]
TaS_2[65]	Size: ~110 nm	PEG	Liver, kidneys	N.A.	FL imaging, CT
TiS_2[66]	Size: ~102 nm	PEG	Liver, spleen	Slow	ICP
MoSe[20]	Size: ~130 nm Thickness: ~1.5 nm	Red blood cells	Spleen, liver	N.A.	Atomic fluorescence spectrometer, ICP
ZrB_2[74]	Size: ~150 nm Thickness: ~7.4 nm	Hyaluronic acid	Liver, spleen	N.A.	FL imaging, PA imaging, ICP
$FePS_3$[75]	Size: 78–154 nm Thickness: 2.9–8.9 nm	poly(vinylpyrrolidone)	Spleen, lung	N.A.	ICP
WS_2/carbon dot[24]	Size: 168 nm Thickness: 2.5–3.0 nm	N.A.	Liver	N.A.	FL imaging
Ti_3C_2/Au[27]	Size: ~260 nm Thickness: ~60 nm	PEG	Liver, spleen, lungs	N.A.	ICP, CT, PA imaging
GO/Fe_3O_4[29]	Size: ~166.6 nm	PEG	Spleen, liver, heart, kidneys	N.A.	ICP, MR imaging

Xenes, MoS_2, and Nb_2C nanosheets. The biological effects of their degradation products are worthy of attention. Others, including graphene derivatives, boron, WS_2 and TiS_2 nanosheets, degrade slowly, which is accompanied by long-term retention and potential toxicity. Notably, nanosheets may undergo morphological reconfiguration *in vivo* due to the unique 2D planar structure. Consequently, some developments on the *in vivo* behavior of nanoparticles may not be suitable for 2D materials, such as the optimal size for passively targeting tumors.

4.2 Future prospects

Numerous scientists have devoted themselves to the investigation and improvement of the *in vivo* behavior of 2D materials. However, the current progress is still far from sufficient to meet the needs of clinical applications. There is still a lack of unified evaluation standards in this field, which are manifested in the following aspects: (1) biological models have been shown to significantly affect the biodistribution of 2D materials, which makes it difficult to compare different studies. (2) There are evident differences in the data obtained by different tracking methods. Even within the same study, different detection methods show qualitative rather than quantitatively consistency in most cases. (3) 2D materials with different preparation processes, sizes, shapes, and modification methods will have completely different performances under physiological conditions, which cannot be simply classified by material types. To realize

the clinical application of 2D materials as soon as possible, it is necessary to establish a scientific evaluation standard for the fate of 2D materials through the cooperation of cross-field experts. In addition, as the most commonly used method for preparing 2D materials in the field of biological applications, liquid phase exfoliation cannot obtain materials with uniform size and shape. The prerequisite for stable therapeutic and metabolic results is to develop a large-scale stable exfoliation method. The bottom-up method in the liquid phase, such as the wet chemical method is a promising path, which has been used for the fabrication of a variety of 2D materials. After establishing unified evaluation standards for 2D nanomedicines, proving the long-term safety of 2D materials is the key to accelerating clinical development. To achieve this goal, extensive standardized animal experiments are essential. In addition, compared to abundant experiments based on small rodents, long-term experiments based on large animals, which enable the investigation of the actual therapeutic effects and metabolic pathways of 2D materials, are relatively few. Furthermore, many efforts have been devoted to developing degradable 2D materials for their biomedical applications. However, the *in vivo* degradation process of 2D materials is often accompanied by drastic changes in the local microenvironment. So, their long-term damage to normal tissue needs to be evaluated carefully and systematically. Also, a safe dosage of 2D materials and their metabolism are an overlooked problem. Although there is still a lot of work to be done, the current progress of 2D materials in the biomedical field is exciting and promising. As ideal candidates for personalized therapy, specific 2D material-based therapeutic strategies have been used for different disease treatments to overcome the limitations of traditional therapies. For example, very recently, there have been clinical trials of graphene in reproductive medicine (trial registration number NCT04881877) and dentistry (trial registration number NCT05341245).

5. Conclusions

2D materials have been applied in the field of biomedicine for over 10 years, and great progress has been made. To realize the clinical transformation, the interaction between the 2D materials and biological milieu must be carefully investigated. 2D materials have a large specific surface area, abundant chemical active sites, and adjustable band structure. These characteristics provide researchers with the opportunity to control the fate of 2D materials *in vivo* through a variety of methods, such as changing size and composition, surface modification, and external stimulation. Various 2D materials, including graphene and its derivatives, Xenes, MXenes, and TMDs, have their unique biological advantages and *in vivo* behavior. As the first type of 2D materials used in biology, graphene derivatives have long-term retention in the body, which raises concerns about their potential long-term toxicity. In contrast, the biodegradability of BP nanosheets is so fast that some strategies have been developed to delay its degradation. Furthermore, most other Xenes likewise have good biodegradability, and were developed for treatment and diagnosis. MXenes are another type of 2D material prepared by selective etching assisted liquid phase exfoliation. Although there are similar preparation processes, different MXenes exhibit different *in vivo* behaviors and biological applications due to differences in components. Similar to MXenes, members of the TMD family also exhibit completely different biological characteristics. Research on the long-term fate of 2D materials *in vivo* is difficult but meaningful. More efforts must be made to understand and control their degradability, clearance, and biodistribution.

Conflicts of interest

There are no conflicts to declare.

Acknowledgements

This work was supported by the National Natural Science Fund (Grant No. 51972055, 81803480, 81960334, and 22004087), the Shenzhen Bay Laboratory Open Program (SZBL2020090501002), the Common University Innovation Team Project of Guangdong (Grant no. 2021KCXTD041), the Guangdong Basic and Applied Basic Research Foundation (2019A1515110926, 2020A1515010787), the Shenzhen Science and Technology Innovation Commission (JCYJ20190809145601651), and the Natural Science Foundation of Top Talent of SZTU (20200201, 20200202, and GDRC202116).

Notes and references

1 K. Yang, J. Wan, S. Zhang, Y. Zhang, S.-T. Lee and Z. Liu, *ACS Nano*, 2011, **5**, 516.
2 Y. Duo, Y. Huang, W. Liang, R. Yuan, Y. Li, T. Chen and H. Zhang, *Adv. Funct. Mater.*, 2019, **30**, 1906010.
3 H. Wang, X. Yang, W. Shao, S. Chen, J. Xie, X. Zhang, J. Wang and Y. Xie, *J. Am. Chem. Soc.*, 2015, **137**, 11376.
4 M. Luo, T. Fan, Y. Zhou, H. Zhang and L. Mei, *Adv. Funct. Mater.*, 2019, **29**, 1808306.
5 W. Poon, B. R. Kingston, B. Ouyang, W. Ngo and W. C. W. Chan, *Nat. Nanotechnol.*, 2020, **15**, 819.
6 L. Newman, D. A. Jasim, E. Prestat, N. Lozano, I. de Lazaro, Y. Nam, B. M. Assas, J. Pennock, S. J. Haigh, C. Bussy and K. Kostarelos, *ACS Nano*, 2020, **14**, 10168.
7 D. A. Jasim, S. Murphy, L. Newman, A. Mironov, E. Prestat, J. McCaffrey, C. Menard-Moyon, A. F. Rodrigues, A. Bianco, S. Haigh, R. Lennon and K. Kostarelos, *ACS Nano*, 2016, **10**, 10753.
8 S. Wilhelm, A. J. Tavares, Q. Dai, S. Ohta, J. Audet, H. F. Dvorak and W. C. W. Chan, *Nat. Rev. Mater.*, 2016, **1**, 16014.
9 K. M. Tsoi, S. A. MacParland, X. Z. Ma, V. N. Spetzler, J. Echeverri, B. Ouyang, S. M. Fadel, E. A. Sykes, N. Goldaracena, J. M. Kaths, J. B. Conneely, B. A. Alman, M. Selzner, M. A. Ostrowski, O. A. Adeyi, A. Zilman, I. D. McGilvray and W. C. Chan, *Nat. Mater.*, 2016, **15**, 1212.
10 H. Soo Choi, W. Liu, P. Misra, E. Tanaka, J. P. Zimmer, B. Itty Ipe, M. G. Bawendi and J. V. Frangioni, *Nat. Biotechnol.*, 2007, **25**, 1165.

11 T. Cao, P. You, X. Zhou, J. Luo, X. Xu, Z. Zhou, S. Yang, Y. Zhang, H. Yang and M. Wang, *J. Mater. Chem. B*, 2016, **4**, 6446.
12 J. Shao, H. Xie, H. Huang, Z. Li, Z. Sun, Y. Xu, Q. Xiao, X. F. Yu, Y. Zhao, H. Zhang, H. Wang and P. K. Chu, *Nat. Commun.*, 2016, **7**, 12967.
13 Q. Liu, T. Fan, Y. Zheng, S. L. Yang, Z. Yu, Y. Duo, Y. Zhang, D. Adah, L. Shi, Z. Sun, D. Wang, J. Xie, H. Wu, Z. Wu, C. Ge, L. Qiao, C. Wei, L. Huang, Q. Yan, Q. Yang, S. Bao, L. P. Liu and H. Zhang, *Nanoscale*, 2020, **12**, 19939.
14 Y. Wang, J. Xie, J. Kang, W. Choi, P. Jangili, B. Zhang, N. Xie, G. Nie, J. He, H. Zhang, L. Liu and J. S. Kim, *Adv. Funct. Mater.*, 2020, **30**, 2003338.
15 R. Cai and C. Chen, *Adv. Mater.*, 2019, **31**, e1805740.
16 H. Kim, J. Kim, M. Lee, H. C. Choi and W. J. Kim, *Adv. Healthcare Mater.*, 2016, **5**, 1918–1930.
17 W. Tao, X. Ji, X. Zhu, L. Li, J. Wang, Y. Zhang, P. E. Saw, W. Li, N. Kong, M. A. Islam, T. Gan, X. Zeng, H. Zhang, M. Mahmoudi, G. J. Tearney and O. C. Farokhzad, *Adv. Mater.*, 2018, **30**, e1802061.
18 X. Zeng, M. Luo, G. Liu, X. Wang, W. Tao, Y. Lin, X. Ji, L. Nie and L. Mei, *Adv. Sci.*, 2018, **5**, 1800510.
19 Z. Sun, Y. Zhao, Z. Li, H. Cui, Y. Zhou, W. Li, W. Tao, H. Zhang, H. Wang, P. K. Chu and X. F. Yu, *Small*, 2017, **13**, 1602896.
20 L. He, T. Nie, X. Xia, T. Liu, Y. Huang, X. Wang and T. Chen, *Adv. Funct. Mater.*, 2019, **29**, 1901240.
21 L. Mei, D. Ma, Q. Gao, X. Zhang, W. Fu, X. Dong, G. Xing, W. Yin, X. Gu and Y. Zhao, *Mater. Horiz.*, 2020, **7**, 1834.
22 Z. Tu, I. S. Donskyi, H. Qiao, Z. Zhu, W. E. S. Unger, C. P. R. Hackenberger, W. Chen, M. Adeli and R. Haag, *Adv. Funct. Mater.*, 2020, **30**, 2000933.
23 S. Tang, C. Peng, J. Xu, B. Du, Q. Wang, R. D. Vinluan, M. Yu, M. J. Kim and J. Zheng, *Angew. Chem., Int. Ed.*, 2016, **55**, 16039–16043.
24 B. Geng, H. Qin, W. Shen, P. Li, F. Fang, X. Li, D. Pan and L. Shen, *Chem. Eng. J.*, 2020, **383**, 123102.
25 L. Cheng, J. Liu, X. Gu, H. Gong, X. Shi, T. Liu, C. Wang, X. Wang, G. Liu, H. Xing, W. Bu, B. Sun and Z. Liu, *Adv. Mater.*, 2014, **26**, 1886.
26 H. Huang, L. He, W. Zhou, G. Qu, J. Wang, N. Yang, J. Gao, T. Chen, P. K. Chu and X. F. Yu, *Biomaterials*, 2018, **171**, 12.
27 W. Tang, Z. Dong, R. Zhang, X. Yi, K. Yang, M. Jin, C. Yuan, Z. Xiao, Z. Liu and L. Cheng, *ACS Nano*, 2019, **13**, 284–294.
28 W. Liang, D. Wang, X. Ren, C. Ge, H. Wang, Z. Li, Q. Liu, M. Qiu, Z. Du, X. Qi, Y. Xu, L. Liu, S. Bao and H. Zhang, *Nanophotonics*, 2020, **9**, 3023–3034.
29 X. Liu, B. Yan, Y. Li, X. Ma, W. Jiao, K. Shi, T. Zhang, S. Chen, Y. He, X. J. Liang and H. Fan, *ACS Nano*, 2020, **14**, 1936–1950.
30 H. Lee, J. Kim, J. Lee, H. Park, Y. Park, S. Jung, J. Lim, H. C. Choi and W. J. Kim, *Biomaterials*, 2020, **263**, 120402.
31 S. Xiong, Z. Li, Y. Liu, Q. Wang, J. Luo, X. Chen, Z. Xie, Y. Zhang, H. Zhang and T. Chen, *Biomaterials*, 2020, **260**, 120339.
32 L. Jin, P. Hu, Y. Wang, L. Wu, K. Qin, H. Cheng, S. Wang, B. Pan, H. Xin, W. Zhang and X. Wang, *Adv. Mater.*, 2020, **32**, 1906050.
33 D. Kim, J. M. Yoo, H. Hwang, J. Lee, S. H. Lee, S. P. Yun, M. J. Park, M. Lee, S. Choi, S. H. Kwon, S. Lee, S. H. Kwon, S. Kim, Y. J. Park, M. Kinoshita, Y. H. Lee, S. Shin, S. R. Paik, S. J. Lee, S. Lee, B. H. Hong and H. S. Ko, *Nat. Nanotechnol.*, 2018, **13**, 812.
34 J. Xie, Z. Shen, Y. Anraku, K. Kataoka and X. Chen, *Biomaterials*, 2019, **224**, 119491.
35 W. Fu, X. Zhang, L. Mei, R. Zhou, W. Yin, Q. Wang, Z. Gu and Y. Zhao, *ACS Nano*, 2020, **14**, 10001.
36 C. Dai, S. Zhang, Z. Liu, R. Wu and Y. Chen, *ACS Nano*, 2017, **11**, 9467.
37 W. Chen, J. Wang, W. Du, J. Wang, L. Cheng, Z. Ge, S. Qiu, W. Pan, L. Song, X. Ma and Y. Hu, *ACS Appl. Nano Mater.*, 2021, **4**, 7963.
38 S. Sadekar, O. Linares, G. Noh, D. Hubbard, A. Ray, M. Janat-Amsbury, C. M. Peterson, J. Facelli and H. Ghandehari, *Drug Delivery Transl. Res.*, 2013, **3**, 260.
39 H. Bai, W. Jiang, G. P. Kotchey, W. A. Saidi, B. J. Bythell, J. M. Jarvis, A. G. Marshall, R. A. Robinson and A. Star, *J. Phys. Chem. C*, 2014, **118**, 10519.
40 S. Chen, C. Xiong, H. Liu, Q. Wan, J. Hou, Q. He, A. Badu-Tawiah and Z. Nie, *Nat. Nanotechnol.*, 2015, **10**, 176.
41 S. Syama, W. Paul, A. Sabareeswaran and P. V. Mohanan, *Biomaterials*, 2017, **131**, 121.
42 X. Wang, Y. Hu, J. Mo, J. Zhang, Z. Wang, W. Wei, H. Li, Y. Xu, J. Ma, J. Zhao, Z. Jin and Z. Guo, *Angew. Chem., Int. Ed.*, 2020, **59**, 5151.
43 W. Tao, X. Zhu, X. Yu, X. Zeng, Q. Xiao, X. Zhang, X. Ji, X. Wang, J. Shi, H. Zhang and L. Mei, *Adv. Mater.*, 2017, **29**, 1603276.
44 J. Hou, H. Wang, Z. Ge, T. Zuo, Q. Chen, X. Liu, S. Mou, C. Fan, Y. Xie and L. Wang. *Nano Lett.*, 2020, **20**, 1447.
45 K. Hu, L. Xie, Y. Zhang, M. Hanyu, Z. Yang, K. Nagatsu, H. Suzuki, J. Ouyang, X. Ji, J. Wei, H. Xu, O. C. Farokhzad, S. H. Liang, L. Wang, W. Tao and M. R. Zhang, *Nat. Commun.*, 2020, **11**, 2778.
46 W. Zhou, T. Pan, H. Cui, Z. Zhao, P. K. Chu and X.-F. Yu, *Angew. Chem., Int. Ed.*, 2019, **58**, 769.
47 X. Shao, Z. Ding, W. Zhou, Y. Li, Z. Li, H. Cui, X. Lin, G. Cao, B. Cheng, H. Sun, M. Li, K. Liu, D. Lu, S. Geng, W. Shi, G. Zhang, Q. Song, L. Chen, G. Wang, W. Su, L. Cai, L. Fang, D. T. Leong, Y. Li, X. F. Yu and H. Li, *Nat. Nanotechnol.*, 2021, **16**, 1150–1160.
48 Z. Sun, H. Xie, S. Tang, X. F. Yu, Z. Guo, J. Shao, H. Zhang, H. Huang, H. Wang and P. K. Chu, *Angew. Chem., Int. Ed.*, 2015, **54**, 11526.
49 C. Gibaja, D. Rodriguez-San-Miguel, P. Ares, J. Gómez-Herrero, M. Varela, R. Gillen, J. Maultzsch, F. Hauke, A. Hirsch, G. Abellán and F. Zamora, *Angew. Chem., Int. Ed.*, 2016, **55**, 14345.
50 Y. Duo, Z. Xie, L. Wang, N. Mahmood Abbasi, T. Yang, Z. Li, G. Hu and H. Zhang, *Coord. Chem. Rev.*, 2021, **427**, 213549.
51 X. Ji, N. Kong, J. Wang, W. Li, Y. Xiao, S. T. Gan, Y. Zhang, Y. Li, X. Song, Q. Xiong, S. Shi, Z. Li, W. Tao, H. Zhang, L. Mei and J. Shi, *Adv. Mater.*, 2018, **30**, e1803031.
52 C. Feng, J. Ouyang, Z. Tang, N. Kong, Y. Liu, L. Fu, X. Ji, T. Xie, O. C. Farokhzad and W. Tao, *Matter*, 2020, **3**, 127.

53 J. Ouyang, C. Feng, X. Ji, L. Li, H. K. Gutti, N. Y. Kim, D. Artzi, A. Xie, N. Kong, Y. N. Liu, G. J. Tearney, X. Sui, W. Tao and O. C. Farokhzad, *Angew. Chem., Int. Ed.*, 2019, **58**, 13405.
54 Y. Wang, W. Feng, M. Chang, J. Yang, Y. Guo, L. Ding, L. Yu, H. Huang, Y. Chen and J. Shi, *Adv. Funct. Mater.*, 2020, **31**, 2005093.
55 H. Lin, X. Wang, L. Yu, Y. Chen and J. Shi, *Nano Lett.*, 2017, **17**, 384.
56 H. Lin, S. Gao, C. Dai, Y. Chen and J. Shi, *J. Am. Chem. Soc.*, 2017, **139**, 16235.
57 X. Ren, M. Huo, M. Wang, H. Lin, X. Zhang, J. Yin, Y. Chen and H. Chen, *ACS Nano*, 2019, **13**, 6438.
58 H. Huang, R. Jiang, Y. Feng, H. Ouyang, N. Zhou, X. Zhang and Y. Wei, *Nanoscale*, 2020, **12**, 1325.
59 H. Lin, Y. Wang, S. Gao, Y. Chen and J. Shi, *Adv. Mater.*, 2018, **30**(4), 1703284.
60 M. Naguib, M. Kurtoglu, V. Presser, J. Lu, J. Niu, M. Heon, L. Hultman, Y. Gogotsi and M. W. Barsoum, *Adv. Mater.*, 2011, **23**, 4248–4253.
61 D. Yim, D. E. Lee, Y. So, C. Choi, W. Son, K. Jang, C. S. Yang and J. H. Kim, *ACS Nano*, 2020, **14**, 10324.
62 T. Liu, S. Shi, C. Liang, S. Shen, L. Cheng, C. Wang, X. Song, S. Goel, T. E. Barnhart, W. Cai and Z. Liu, *ACS Nano*, 2015, **9**, 950.
63 J. Xue, H. Liu, S. Chen, C. Xiong, L. Zhan, J. Sun and Z. Nie, *Sci Adv*, 2018, **4**, eaat9039.
64 J. Black, *Clin. Mater.*, 1994, **16**, 167.
65 Y. Liu, X. Ji, J. Liu, W. W. L. Tong, D. Askhatova and J. Shi, *Adv. Funct. Mater.*, 2017, **27**, 1703261.
66 J. Hao, G. Song, T. Liu, X. Yi, K. Yang, L. Cheng and Z. Liu, *Adv. Sci.*, 2017, **4**, 1600160.
67 H. Huang, W. Feng, Y. Chen and J. Shi, *Nano Today*, 2020, **35**, 100972.
68 C. Dou, N. Ding, F. Luo, T. Hou, Z. Cao, Y. Bai, C. Liu, J. Xu and S. Dong, *Adv. Sci.*, 2018, **5**, 1700578.
69 X. Qi, H. Liu, W. Guo, W. Lin, B. Lin, Y. Jin and X. Deng, *Adv. Funct. Mater.*, 2019, **29**, 1902235.
70 A. C. Ip, B. Liu, P. J. Huang and J. Liu, *Small*, 2013, **9**, 1030.
71 W. Jiang, Z. Zhang, Q. Wang, J. Dou, Y. Zhao, Y. Ma, H. Liu, H. Xu and Y. Wang, *Nano Lett.*, 2019, **19**, 4060.
72 Y. Lin, Y. Wu, R. Wang, G. Tao, P.-F. Luo, X. Lin, G. Huang, J. Li and H.-H. Yang, *Chem. Commun.*, 2018, **54**, 8579.
73 W. Feng, R. Wang, Y. Zhou, L. Ding, X. Gao, B. Zhou, P. Hu and Y. Chen, *Adv. Funct. Mater.*, 2019, **29**, 1901942.
74 D. Chen, Z. Jin, B. Zhao, Y. Wang and Q. He, *Adv. Mater.*, 2021, **33**, e2008089.
75 Q. Zhang, Q. Guo, Q. Chen, X. Zhao, S. J. Pennycook and H. Chen, *Adv. Sci.*, 2020, **7**, 1902576.